Landslides as geological hotspots of CO₂ emission: clues from the instrumented Séchilienne landslide, Western European Alps.

Pierre Nevers[1], Julien Bouchez[2], Jérôme Gaillardet[2,4], Christophe Thomazo[3], Delphine Charpentier[1], Laëticia Faure[2] and Catherine Bertrand[1]

[1]UMR Chrono-Environnement 16 route de Gray, 25000 Besançon, France
[2]Université de Paris, Institut de physique du globe de Paris, CNRS, F-75005 Paris, France
[3]UMR CNRS/uB6282 Biogéosciences 6 Boulevard Gabriel, 21000 Dijon, France
[4]Institut Universitaire de France, 75231 Paris, France

Correspondence to: Pierre Nevers (*pierre.nevers@univ-fcomte.fr*)

Abstract. This study makes use of a highly instrumented active landslide observatory (9 years of data) in the French Alps, the Séchilienne slope. Here we use a combination of major element chemistry and isotopes ratios ($^{87}Sr/^{86}Sr$, $\delta^{34}S$) measured in different water types of the stable and unstable part of the Séchilienne instability to assess the contribution of the different lithologies of the slope and the chemical weathering mechanisms. Chemical and isotopic ratios are used to characterize weathering processes and the origin of waters and their flowpaths through the massif. A mixing model allows us to allocate the different major elements to different sources, to identify secondary carbonate formation as a major process affecting solutes in the subsurface waters of the instability, and to quantify the involvement of sulfuric and carbonic acids as a source of protons.

We show that the instability creates favorable and sustained conditions for the production of sulfuric acid by pyrite oxidation, by opening new fractures and supplying fresh reactive surfaces. We clearly identify the contribution of the dissolution of each mineral phase to the chemistry of the waters, with a clear role of remote gypsum dissolution to the sulfate budget in the sampled waters. We are also able to refine the pre-existing hydrogeological views on the local water circulation and water flow paths in the instability by showing the hydrological connectivity of the different zones. Overall, our results show that the Séchilienne landslide, despite its role in accelerating rock chemical and physical weathering, acts as a geological source of CO₂ to the atmosphere. If generalizable to other large instabilities in mountain ranges, this study illustrates the complex coupling between physical and chemical erosion and their impact on the carbon cycle and global climate. The study also highlights the importance of distinguishing between sulfite oxidation and gypsum dissolution as a source of sulfate ions to rivers, particularly in mountain ranges.

1 Introduction

The weathering of rocks plays a key role in the chemical and climatic evolution of the Earth surface and is one of the geological processes that impacts atmospheric CO₂ concentration. When carbonic acid is the proton supplier, silicate weathering removes carbon dioxide from the atmosphere (Lerman et al., 2007, Berner and Berner, 2012). However, the oxidative dissolution of sulfides (*e.g.* pyrite FeS_2) produces sulfuric acid that can act as an alternative proton supplier to chemical weathering reactions. Although not directly influencing atmospheric CO₂, silicate weathering by sulfuric acid does reduce the potential of rock weathering for CO₂ sequestration by "removing" silicates from the Earth surface and thus limiting their weathering by carbonic acid. When sulfuric acid reacts with carbonate minerals, dissolved inorganic carbon is added to ambient waters which leads on the long term to CO₂ release towards the atmosphere (Lerman et al., 2007, Calmels et al., 2007, S.-L. Li et al., 2008, Torres et al., 2014). The relevance of this process for the global carbon cycle is two-fold.

First, even though carbonate rocks do not constitute the major fraction of the rock types exposed at the Earth surface, the dissolved products of carbonate dissolution dominate global weathering fluxes (Gaillardet et al., 1999) as carbonate minerals dissolve several orders of magnitude faster than silicates (Lasaga 1984). Second, because weathering by sulfuric acid is mainly limited by the supply of sulfide minerals to the Earth surface, it is particularly prominent in active mountain belts characterized by high erosion rates (Calmels et al., 2007; Torres et al., 2016; Blattmann et al., 2019). Within these tectonically active environments, landslides are likely to be hotspots of sulfuric acid production, carbonate weathering, and CO_2 release (Emberson et al., 2015, 2018). Indeed, slope instability leads to sustained grain comminution and fractures opening, thereby providing a continuous supply of contact surfaces between water, air, and minerals that can in particular allow for sulfuric acid production and carbonate mineral weathering (Binet et al., 2009; Bertrand et al., 2014).

Here we explore the hypothesis that slope instability can constitute a mechanism promoting coupled sulfide oxidation and carbonate weathering, in a contribution to the study of the role active mountain ranges play on the global carbon cycle (Raymo and Ruddiman, 1992; Hilton and West, 2020). We focus on the Séchilienne slope instability located in the French Alps. This site of active, slow landsliding serves as an observatory for landslide processes and has been the subject of previous hydrogeological and geophysical investigation (Vengeon, 1998; Guglielmi et al., 2002; Meric et al., 2005; LeRoux et al., 2011; Vallet et al., 2015; Lajaunie et al., 2019). We combine measurements of the concentration of major elements and of the isotope composition of strontium and sulfur ($^{87}Sr/^{86}Sr$, $\delta^{34}S$) dissolved in groundwater and springs to estimate the contribution of different rock types to the dissolved species produced by weathering reactions in the landslide. In particular, we estimate the relative role of different acid types (carbonic *vs.* sulfuric) and of two rock types (silicates *vs.* carbonates), and evaluate the role played by secondary carbonate formation on the solute budget of percolating waters. Besides shedding light on the global impact of landsliding on atmospheric CO_2, Sr and S isotopes coupled to water chemistry allow for a quantitative analysis of solute sources in natural waters and of the chemical evolution of natural waters, which in turn opens the possibility to improve existing hydrogeological model in complex environments such as landslides.

2 Study area

2.1 Geological setting

The "Séchilienne" site hosts a highly-instrumented, continuously-monitored landslide, part of the French National Landslide Observatory (OMIV, http://www.ano-omiv.cnrs.fr/). The Séchilienne massif is located at the SW border of the Paleozoic crystalline Belledonne mountain range in the French Alps, 20 km southeast of Grenoble (Isère, France; Fig. 1). The active zone of the site is a gravitational instability affecting 60.10^6 m^3 of material, with a maximum depth of about 150 m, located on a south-facing slope of the massif (Le Roux et al. 2011). The most active part of the landslide, referred to as "les Ruines", is located on the eastern border of the unstable zone. Long-term monitoring (extensometers, geodetic measurements, tacheometers and microwave radar) shows that the displacement velocity is around 300 cm y^{-1}, while the less active parts of the site are moving at a mean of 10 cm y^{-1} (Le Roux et al. 2011; Dubois et al. 2014).

Geological and structural information are provided by the geological map and by two boreholes drilled in 2010 in the unstable area at depths down to 150 m. Baudement et al. (2013) has integrated these information in a GOCAD® 3D model, recently used by Lajaunie et al. (2019) to propose a new vision of the Séchilienne slope based on a 3D resistivity model. The basement of the massif is mainly composed of micaschists showing a N-S trending sub-vertical foliation. Stratigraphically discordant deposits dating from the Carboniferous to the Liassic periods cover the micaschists on the top north – northeast of the massif (Mont Sec) and along the Sabot Fault (Fig. 1). The slope is locally covered by Quaternary (Würm) glacio-fluvial deposits made of material reworked from the surrounding formations (Vengeon 1998, Vallet 2014). The micaschists consist primarily of quartz, biotite, phengite, and chlorite with occurrence of carbonate veins and pyrite in fractures. Carboniferous deposits are made of black shales, sandstones, and conglomerates with quartz and serpentine pebbles. Triassic rocks

correspond to sandstone, quartzite, dolomite and locally of black shales, argilites, and gypsum. Liassic deposits are limestones with intercalation of layers rich in breccia consisting of micaschist, dolomite, and coal (Barféty et al. 1972, Vengeon 1998, Vallet 2014). Strong local heterogeneities exist in terms of lithology and fracturation and are induced by the gravitational deformation (Lajaunie et al. 2019).

85   The part of the slope affected by the landslide extends from 400 m to 1,100 m above sea level (a.s.l.; Le Roux et al. 2011; Fig. 1d). Above the elevation of 1,100 m a.s.l., the morphology of the Mont Sec corresponds to a plateau of glacial origin underlain by moraine deposits concentrated in small topographic depressions. The landslide is delimited at its northern border by a major head scarp of about 10 meters high and several hundreds of meters wide, which separates the glacial plateau of Mont Sec from the unstable zone. Eastward, N-S faults scarps limit the landslide whereas the western and

90   southern parts are not well defined by geomorphological evidence. The motion of the landslide consists in a deeply-rooted, toppling movement with N50-70 slabs toward the valley, coupled with the sagging of the upper zone of the slope near the Mont Sec (Vengeon 1998). The Séchilienne instability is assumed to originate from the decompression of the basement rocks after the Romanche glacier retreated at the last glaciation (15 kyr ago). Decompression caused the opening of fractures and then the collapse of the summit of the Mont Sec (Montjuvent and Winistorfer 1980, Vengeon et al. 1999, Potherat and

95   Alfonsi, 2001,). The Séchilienne slope is thus affected by a dense network of near-vertical, open fractures trending N70 and N110/120, controlling the deformation of the Séchilienne landslide which is characterized by a deep progressive deformation (about 100-150 m) and the absence of a well-defined basal sliding surface. Two N20 major fractures are also crossing the Séchilienne massif and the Sabot and Séchilienne faults. Open fractures are locally filled with detrital material resulting from the erosion of the massif (Vallet et al. 2015a).

100 Borehole logs available within the instability (Lajaunie et al. 2019) show that the rock formations below the slope are relatively unstructured, and that pyrite is heterogeneously distributed therein. Rock samples along the boreholes seem to have been subjected to oxidizing conditions, albeit with no clear sulfide reaction front at the scale of the instability. In addition, petrological observations on thin sections from these boreholes, combined with mineralogical analyses obtained from X-ray diffraction (XRD; supplementary materials, section 1) show that pyrite is disseminated within the rocks, with no

105 particular association with calcite. Gypsum was not detected from XRD analyses in the sampled rocks, consistent with results from inverse modeling by Vallet et al. (2015) suggesting that sulfate in waters from the unstable zone (UZ) essentially originates from pyrite oxidative weathering.
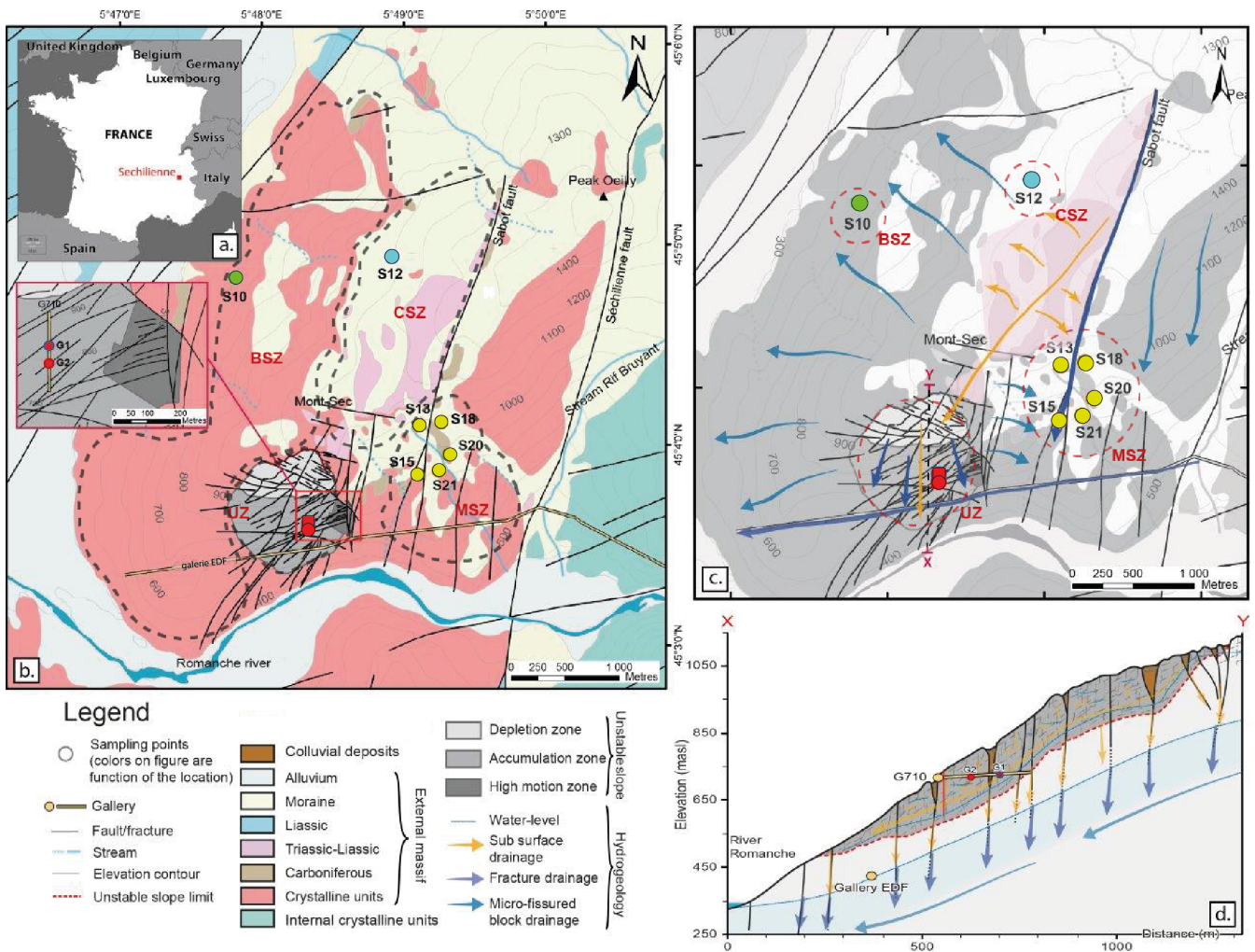
Figure 1: Map of the Séchilienne site a. Location of the Séchilienne massif in the French Alps, b. Simplified geological map of the Séchilienne massif and sampling locations, c. schematic hydrogeological model of the Séchilienne massif, d. hydrogeological cross-section of the instability, modified after Vallet et al. (2015).

2.2 Hydrogeological setting

The high degree of fracturation and heterogeneity of the Séchilienne massif leads to distinct and complex patterns of hydrological flow paths. At Séchilienne, water pathways are characterized by different transit times related to a dual permeability behavior that is typical of fractured rock aquifers where conductive fractures play a major role in the drainage (Fig 1.c): rapid transit of infiltration waters through fractures reflects the functioning of a so-called "reactive" hydrological component, whereas slower transit of water through the micro-fissured, less permeable rock matrix, resulting in a smeared response of flow rate to rainfall, typifies an "inertial" circulation (Maréchal 1998, Cappa et al. 2004, Vallet et al. 2015a). In particular, the Sabot and Séchilienne faults play an important role on fluid flow through the massif by draining waters from the sedimentary cover at a fast rate (0.7 km day^{-1}), and bypassing the less pervious and more inertial micro-fissured matrix characterized by lower flow velocity (0.08 km day^{-1}) (Mudry et Etievant 2007; Vallet et al. 2015a). Local perched aquifers develop during high-flow periods and discharge downwards to the main aquifer, due to the contrast of permeability between the decompressed zone at the surface and the unaltered rock (Lajaunie et al., 2019). An underground tunnel for the production of electricity in a local hydropower plant, named "Galerie EDF", built by Electricité de France (EDF) and located at the base of the slope, acts as a major westward drain for groundwater (Vallet et al. 2015a).

Difference in hydraulic conductivity between the highly fractured unstable zone (thickness about 150-200 m, Le Roux et al. 2011) and the basement situated under the landslide (Fig 1.d) led to the build-up of a two-layer aquifer system. Those two

layers are connected to one another through major fractures (Vengeon 1998, Meric et al. 2005; Le Roux et al. 2011, Guglielmi et al. 2002, Vallet et al. 2015a). A temporary and discontinuous shallow perched aquifer is present in the landslide with extension and connectivity varying according to short-term recharge variations. This aquifer is almost dry during the low flow periods, with numerous disconnected saturated pockets (such as open fractures filled by colluvial deposit and altered material) linked to the heterogeneity of the landslide (Guglielmi 2002, Cappa et al. 2004, Vallet et al. 2015a). The recharge of this aquifer is mainly local (through trenches and counterscarps, limiting the runoff) with a contribution of remote groundwater through near-surface drainage at high-flow periods from the sedimentary cover above the landslide (near the Mont Sec summit) (Guglielmi 2002, Vallet et al. 2015a). The deep aquifer, which extends all over the massif (altitude around 550 m asl), corresponds to a saturated layer hosted by the fractured metamorphic bedrock and to an overlying, 100-m thick vadose layer (Vallet et al. 2015a). The deep aquifer level is controlled by the constant water heads of the Romanche alluvium in the valley, and of the Galerie EDF (425 m a.s.l.).

3. Samples and analytical methods

Nine outflows draining the whole massif were investigated for physico-chemical parameters and dissolved load chemistry (Fig 1.a). Two of these outflows (G1 and G2) are located within the Unstable Zone (UZ) and correspond to seep water collected in a tunnel excavated to monitor the landslide at 710 m a.s.l. (G710). The remaining outflows (S10, S12, S13, S15, S18, S20, S21) correspond to springs draining the Stable Zone (Fig 1.a). These outflows can be differentiated regarding the dominant local lithology: S10 is located in the Bedrock Stable Zone (BSZ), S12 in the Carbonate Stable Zone (CSZ), and S13, S15, S18, S20, and S21 are located in an area of the Stable Zone characterized by mixed lithology (Mixed Stable Zone, MSZ). Samples were collected every three months over the period 2010-2019. Between 2014 and 2017, waters were sampled once a year for Sr isotopes, while samples for S isotope were collected in 2019. In total, 360 water samples were collected and analyzed for this study. Four local rocks samples were taken, reflecting the main lithological types encountered at Séchilienne: basement micaschist, carbonate (both calcite-rich and dolomite-rich) from the sedimentary cover, and a recrystallized vein in micaschist.

Field measurements of water temperature, pH, and electrical conductivity (EC) were made with a WTW pH/Cond 340i (Xylem Inc.) sensor, with a precision of 0.1 unit and 0.1 μS cm^{-1} for pH and EC, respectively. Water samples were collected in polyethylene bottles and filtered with a 0.45 μm pore diameter nylon filter, before being preserved in cold conditions for measurements of major element concentration and Sr and S isotopes. Analyses of dissolved major elements were all carried out at the research laboratory Chrono-Environnement at the University of Franche-Comté. Dissolved major cation concentrations were measured by atomic absorption spectrometry (AA 100 Perkin-Elmer) with detection limits of 0.5, 0.1, 0.01, and 0.1 mg L^{-1} for Ca^{2+}, Mg^{2+}, Na^+ and K^+, respectively. Dissolved anion concentrations were determined using high-pressure ion chromatography (Dionex DX 100) with detection limits of 0.1, 0.1, and 0.05 mg L^{-1} for Cl^-, SO_4^{2-} and NO_3^-, respectively. The concentration of HCO_3^- was measured by acid titration (N/50 H_2SO_4) within 48 hours after sampling, with 1% accuracy. Dissolved silica concentration was analyzed with a spectrophotometer (Spectroquant, Pharo 300, Merck) using a silica-test kit (Merck) with 3% accuracy. Only analyses with a charge balance better than 10% were taken into account.

Strontium isotope analyses were carried out at the High-Resolution Analytical Platform (PARI) of the Institut de Physique du Globe de Paris (IPGP). For water samples, dissolved Sr was first isolated from the water sample matrix by automated ion chromatography following the method of Meynadier et al. (2006). For rocks, in addition to bulk samples analysis after digestion in concentrated HF and HNO_3. a three-step sequential leaching procedure was conducted using H_2O, 1M acetic acid, and 1M HCl. The first step was designed to recover the exchangeable fraction adsorbed onto the solid surface; step 2 was for extracting Sr from carbonates, amorphous hydroxides, and phosphate minerals (Tessier et al., 1979); step 3 was to dissolve any high-order Fe–Mn oxide/oxyhydroxide phases that might be present after HCl leaching (Tessier et al., 1979).

The leachate solutions and residual samples were measured for major and trace elements by Quadrupole ICP-MS (Agilent 7900) with a precision better than 5% and processed for $^{87}Sr/^{86}Sr$ ratio analysis following the same procedure used for bulk samples. To that effect, 3M HNO_3 aliquots of digestion solutions were loaded on columns loaded with 0.2 mL of Sr-SPEC resin (Eichrom). Then, 3M HNO_3 was used to elute the sample matrix before Sr was eluted in H_2O. Strontium isotope ratios were then measured using a Multi-Collector Inductively Coupled Plasma Mass Spectrometer (MC-ICP-MS; Thermo-Fisher Neptune) in low resolution mode (Hajj et al., 2017). Purified Sr solutions were introduced using an APEX desolvation unit and a PFA nebulizer at a rate of 50 to 100 μL min^{-1} depending on the measurement session, and at Sr concentrations between 50 and 150 ppb. The accuracy and reproducibility of the $^{87}Sr/^{86}Sr$ analysis was assessed using repeated measurements of the international isotope Sr carbonate standard (SRM987, NIST). Over three sessions of measurements, the average value for SRM987 standard NIST was 0.710249 ± 0.000025, in agreement with the accepted value.

Sulfur isotopes measurements were performed at the Biogéosciences Laboratory, University of Bourgogne, Dijon, France on both sulfates from water samples and sulfides from basement micaschist. Nine samples were treated with an excess of 250 g l^{-1} $BaCl_2$ solution to precipitate $BaSO_4$. After centrifugation, the $BaSO_4$ precipitate was washed several times with deionized distilled water and dried at 60°C for 24 hours in an oven. Five hundred micrograms of purified barite samples were poured into tin capsules and homogeneously mixed with 1/3 of vanadium pentoxide before isotopic measurements (^{34}S, ^{32}S) using a Vario PYRO cube (Elementar GmbH) connected online *via* an open-split device to an IsoPrime IRMS system (Isoprime, Manchester, UK). Sulfur isotope data are expressed in delta notation and reported in units per mille (‰). The $\delta^{34}S$ data are reported with respect to the international standard Vienna Cañon Diablo Troilite (VCDT). Analytical errors are ±0.3‰ (1σ) based on replicate analyses of the international barite standard NBS-127, which was used for data correction assuming a $\delta^{34}S$ value of +20.3 on the VCDT scale.

Sulfur contained in sulfides was extracted from eight rock samples of the basement micaschist formation on aliquots of 3 grams (4 sub-samples on each of two rock samples, including unaltered pyrite and iron oxides) following the method described by Canfield et al. (1986). Dried and rinsed Ag_2S precipitates recovered after wet chemistry sulfides extraction are weighted for gravimetric quantification of sample sulfur content. Five hundred micrograms of silver sulfides precipitates were then mixed with an equivalent weight of tungsten trioxide in tin capsules before combustion in a Vario pyro cube (Elementar GmbH^{TM}). Sulfur isotope compositions ($\delta^{34}S$) were measured using an IsoPrime IRMS device (Isoprime, Manchester, UK). International standards (IAEA-S-1, IAEA-S-2, IAEA-S-3) were used for calibration and results are reported in the δ-notation relative to the Vienna Canyon Diablo Troilite (VCDT) standard. Reproducibility (1σ) is better than 0.2‰ based on duplicate analyses of standard materials and samples.

4. Results

The concentration of major and trace elements, as well as Sr and S isotope composition of rock samples are given in Table 1 and 2 (data available at 10.5281/zenodo.4606732). The concentration of major elements, EC, pH, temperature, and Sr and S isotope composition of water samples are given in Table 3.

4.1 Major elements

Rock samples

The two limestone samples show distinctive response to the leaching procedure, with most of the Ca of the "Laffrey" limestone located in the acetic acid leachate (67%) and the rest in the HCl fraction (11%), which is indicative of the calcitic nature of this rock sample (Table 1). By contrast, most of the Ca of the "Lias" sample is hosted in the residue, while a significant fraction (37%) is HCl-soluble, suggesting that the carbonate fraction of this sample is dolomitic. The "micaschist"

and "vein" samples have higher bulk Sr/Ca, Mg/Ca, Al/Ca and Na/Ca ratios than the two limestone samples, confirming that they are mostly made of silicate minerals.

Spring water samples

The chemical composition of waters sampled on the Séchilienne site is very diverse, reflecting heterogeneity in rock types and the existence of various groundwater flow paths. Water pH at Séchilienne is relatively high and varies from 6.5 to 9.4 with a mean value of 7.9. Electrical conductivity range between 79 µS cm^{-1} and 1114 µS cm^{-1} (Table 3). From the major ion perspective, samples can be grouped into 4 main water types (Fig. 2). These water types correspond to those identified previously by Vallet et al. (2015a). Type 1 corresponds to Ca-HCO$_3$ waters, typical of water draining carbonate formations, typified by the S12 spring draining the carbonate cover at the top of the Séchilienne slope (CSZ). S12 has low EC values ranging from 79 µS cm^{-1} to 147 µS cm^{-1} with a mean of 117 µS cm^{-1}. The second group corresponds to Mg-Ca-HCO$_3$ rich waters, which have circulated through the sedimentary cover (carbonate and dolomite) and the micaschists bedrock and is represented by the S10 spring (BSZ). All S10 samples have higher electrical conductivities ranging from to 308 µS cm^{-1} to 509 µS cm^{-1} with a mean of 443 µS cm^{-1}. Waters sampled in the unstable part of the slope (UZ), include the underground outflows G1 and G2 and show a chemical composition that vary from Mg-Ca-HCO$_3$-SO$_4$ waters to Mg-Ca-SO$_4$ waters and constitute the third hydrogeochemical group. The highest EC values of this study are observed for the G1 outflow with electrical resistivities ranging from 613 µS cm^{-1} to 1114 µS cm^{-1} with a mean value of 824 µS cm^{-1}. The other outflow of the unstable zone (outflow G2), in contrast to the previous one, shows a mean electrical conductivity value around 391 µS cm^{-1}, with a minimum value of 313 µS cm^{-1} (and a maximum value of 470 µS cm^{-1}). The fourth and last type of waters include the S13, S15, S18, S20, S21 outflows, sampled in the stable part of the slope (MSZ) along the Sabot fault, and show Ca-Mg-HCO$_3$-SO$_4$ type waters. The MSZ group exhibits EC values ranging from 357 µS cm^{-1} to 567 µS cm^{-1}, with a mean of 479 µS cm^{-1}. Waters of the Unstable Zone group (G1, G2) are characterized by the highest concentrations in SO$_4^{2-}$ (from 1.32 to 3.90 mmol L^{-1}) compared to the other outflows sampled which have values ranging from 0.57 to 1.34 mmol L^{-1} for the MSZ outflows (S13, S15, S18, S20, S21) and from 0.48 to 0.67 for the S10 (BSZ) outflow (Fig. 2; Tab. 3). Fig. 2 clearly shows that SO$_4^{2-}$ ions are significantly contributing to the electrical balance of the analyzed waters. Dissolved Cl$^-$ concentrations are lower than 50 µmol L^{-1} in springs S10, S12, S13, S18, but can reach values above 100 µmol L^{-1} in springs S15, S20, and S21. Dissolved NO$_3^-$ concentrations are typically below 20 µmol L-1 in springs G1, G2, and S10, but are higher in springs S12, S13, S18, S15, S20, and S21, with concentrations above 100 µmol L^{-1} observed in the latter (Tab. 3).

Rainwater samples (Tab. 3) show very low EC values with a mean of 26 µS cm^{-1} and low concentrations for all elements analyzed. In particular, chloride concentrations range from 3.3 µmol L^{-1} to 20.3 µmol L^{-1}.
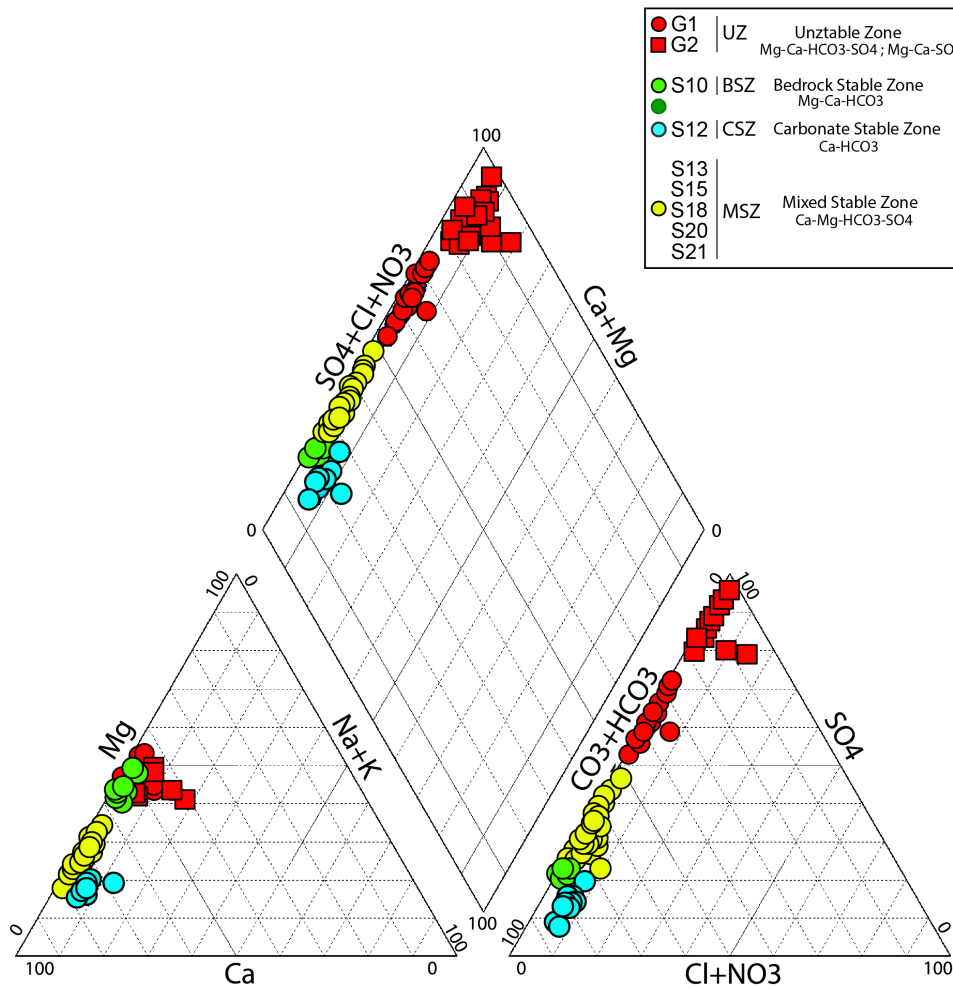
Figure 2: Piper diagram representing the major water types samples in the outflows of the Séchilienne massif

245

4.2 Strontium isotopes

Rock samples

The two carbonate rock samples have the lowest Sr isotopic ratios (Table 1), with the lowest value being 0.7095 slightly higher than the Sr isotopic composition of lower Jurassic seawater (from 0.7065 to 0.7076; Koepnick et al., 1990). The

250   acetic-acid and HCl soluble fractions of the limestone samples, as well as the bulk analysis of the dolomitic "Lias" sample and its H_2O leachate, are characterized $^{87}Sr/^{86}Sr$ ratios of ~ 0.7105. The $^{87}Sr/^{86}Sr$ ratio of all the leachates of the calcitic "Laffrey" sample, as well as of the bulk sample, show a wider range of variation, in the range 0.7104-0.7179. By contrast, the highest $^{87}Sr/^{86}Sr$ ratios were found in the micaschists samples with a value of 0.7351 (Table 1), typical of silicate rocks (0.73±0.01; Négrel et al., 1993). The veins contained in the micaschists also show high Sr isotopic ratios (0.7277). Such high

255    $^{87}Sr/^{86}Sr$ ratios are particularly encountered in the residues and bulk samples.

Spring water samples

The Sr isotope ratios measured in the spring samples in and around the Séchilienne instability range from 0.7093 to 0.7231 (Table 3). The four main groups of waters have contrasted $^{87}Sr/^{86}Sr$ isotopic ratios. The highest $^{87}Sr/^{86}Sr$ values are found in

260   the UZ underground outflows samples (G1, G2) with an average of 0.7210 ± 0.0006 (one standard deviation). The lowest $^{87}Sr/^{86}Sr$ values correspond to the waters of the MSZ (springs S13, S15, S18, S20, and S21), and average at 0.7095 ±

0.00012, *i.e.* at the value measured in the carbonate rock. The S12 outflow (CSZ) is characterized by $^{87}Sr/^{86}Sr$ ratios of around 0.7095 ± 0.00005, *i.e.* close to those of the MSZ group. Intermediate values of Sr isotopic ratios are found for the samples of the BSZ group (S10), with an average of 0.7148 ± 0.00019.

4.3 Sulfur isotopes

Rock samples

Sulfur isotope composition of unaltered rock samples (4 samples) range from -7.9‰ to 17.8‰ with an average value of 1.2‰ $\pm$ 11.8‰, whereas weathered micaschists (4 samples) exhibit $\delta^{34}S$ values ranging from -13.1 to 9.9‰ and an average of -1.4‰ $\pm$ 9.5‰; (Table 2). These numbers show the extremely large range of possible sulfur isotope signals co-existing in the various rock types present in the landslide.

Spring water samples

Waters show a much narrower range of $\delta^{34}S$ values, ranging from -5.5‰ to 6.5‰ (mean 0.43‰ $\pm$ 5.12‰). The highest $\delta^{34}S$ values are observed for water of the MSZ group (outflows S13, S15, S20, S21) with an average of 6.28‰ $\pm$ 0.34‰. Samples of the S12 outflow (CZS group) also exhibits a high $\delta^{34}S$ value of 6.03‰. The G1 and G2 outflows (UZ group) exhibit negative $\delta^{34}S$ values with an average of -3.74 ‰ $\pm$ 1.75‰), with lower $\delta^{34}S$ values for G2, (averaging at -5.33‰ $\pm$ 0.22‰) than for G1 (2.2‰ $\pm$ 0.06‰). The BSZ group (outflow S10) is characterized by $\delta^{34}S$ values that are intermediate between those of the MSZ and UZ groups (2.4‰).

5. Discussion

5.1 Identification of sources to dissolved species

5.1.1 Atmospheric and anthropogenic sources

Rainwater is potentially a significant source of elements to the water sampled in the different springs at Séchilienne. To assess the importance of atmospheric inputs, we use Cl^- concentrations. Chloride is not significantly involved in chemical reactions at the Earth surface and its presence in waters has three main origins: rainwater (through the dissolution of seasalt aerosols), dissolution of saline rocks or inclusions, and anthropogenic inputs. On the other hand, at Séchilienne, NO_3^- is most likely to be derived from human activity, through fertilizer input and/or domestic waste. Therefore, the correlation between Cl^- and NO_3^- concentrations in springs S15, S20, and S21 ($R^2 = 0.65$; Fig. S8; supplementary materials) suggests that beyond rainwater, anthropogenic inputs are a significant Cl^- source to these springs. This inference is consistent with the presence of villages upslope from these springs. High Cl^- concentrations (> 100 µmol L^{-1}) are also found in some samples from underground outflows G1 and G2 (Table 3). However, in the case of these two springs such high Cl^- concentrations are not accompanied with high NO_3^- concentrations but correlate to some extent with dissolved Na^+ and K^+ concentrations (Fig. S8). This observation could be indicative of the dissolution of salts (NaCl and KCl) as a significant process delivering Cl^- and cations to the springs. Although the origin of these salts is unclear, we note that Zn-Pb ore deposits are reported discovered in the bedrock of Séchilienne landslide exploitation (Barnes, 1997). The presence of fluid inclusions containing alkali elements and Cl in these ores is likely, and leaching of such fluid inclusions could have occurred because of the exposure of new mineral surface during ore. To summarize, the excess of Cl in Séchilienne springs is most probably due to a combination of human activity (road salts and agriculture) and to dissolution of fluid inclusions of hydrothermal origin.

The expected concentration of Cl^- derived from precipitation in spring waters (hereafter called [Cl]$_{crit}$ for "critical chloride", Stallard et al., 1983) of the Séchilienne massif can be estimated by multiplying the mean Cl^- concentration found in rainwater by the mean evapotranspiration factor (P/ETP: 4.02 with P: precipitation, ETP: evapotranspiration calculated from

temperature and latitude of the study site, according to Oudin et al. 2005). Alternatively, [Cl]crit can be estimated as being equal to the lowest Cl⁻ concentrations in the sample set (S10, S12 and S21 springs). Both methods concur to fix the atmospheric contribution of Cl⁻ to the Séchilienne waters at a maximum of 30 µmol l⁻¹. Above this concentration, additional sources must be involved. Once [Cl]crit is known, it is possible to correct all cation concentrations from the atmospheric seasalt input by using:

$$[X]^* = [X] - [Cl]_{crit} \times \left(\frac{X}{Cl}\right)_{seawater} \tag{1}$$

In this equation, $[X]^*$ denotes the concentration of an element X in the water sample, corrected from the atmospheric input, and $(X/Cl)_{seawater}$ is the seawater elemental ratio. This correction is only significant for Na⁺, due to the relatively high concentrations found in the Séchilienne waters.

As explained above, significant excess of Cl⁻ ([Cl] > [Cl]crit) is found for the S15, S20, and S21 springs where this excess is the highest (about 30 to 60 µmol l⁻¹) and due to domestic and/or agricultural activity; and in the G1 and G2 underground outflows (between 15-20 µmol l⁻¹ of excess), where this excess can be attributed to salt dissolution. For the first group of springs, it is most likely that input of Cl⁻ is associated with input of K⁺, through the use of fertilizers. For the second group of springs each mole of Cl⁻ released by salt dissolution can be associated with one mole of K⁺ or one mole of Na⁺. Because of the challenge associated to assessing the exact cause for the observed Cl⁻ excess in these springs, in the quantitative source apportionment (section 5.1.4) we use a stochastic approach to reflect the uncertainty linked to the nature of the cations delivered to the springs by these Cl⁻ sources. However, we emphasize that for the springs where silicate weathering is the most prominent process in terms of cation production (G1 and G2; see section 5.1.2 below), the correction for the solute sources causing the Cl⁻ excess (human activity and salt dissolution) is relatively minor.
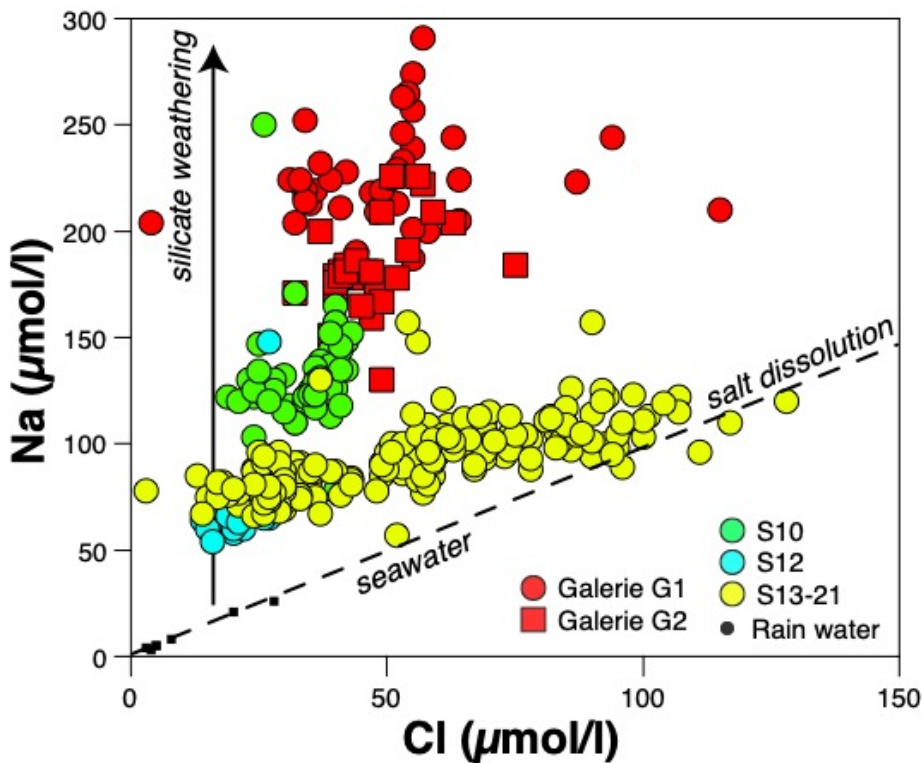
Figure 3: Na vs Cl concentrations measured in the different groups of water outflow from the Séchilienne massif. Rainwater data points are aligned along the seawater composition (seasalts).

5.1.2 The importance of silicate weathering

The concentration of Na$^+$, once corrected from atmospheric and anthropogenic inputs, can be used as a proxy of silicate weathering reactions, if the dissolution of silicate minerals is a dominant source of Na to surface waters compared to salt dissolution and human activity. The underground outflows G1 and G2 have the highest Na* concentrations (mean values 200±30 µmol L^{-1} and 158±21 µmol L^{-1} for G1 and G2, respectively) (Fig. 3). This observation suggests the importance of silicate weathering reactions in the Unstable Zone, made of fractured micaschists. Although as explained above the source of excess chloride could also be contributing Na (were this additional source NaCl inclusions), the Na* concentrations remain the highest found in the Séchilienne landslide area assuming that all Cl$^-$ release to waters is associated to an equivalent Na$^+$ release (in moles). Despite their excess of Cl$^-$, the MSZ outflows chemistry also reveals that silicate weathering reactions are releasing Na$^+$ to those waters (Fig. 3). However, the Na* concentrations of the Mixed Stable Zone (60 µmol L^{-1} on average) are equal to around half of those encountered in the Unstable Zone. This contrast between the stable (MSZ) and unstable zone (UZ) illustrates that the intensity of silicate weathering is linked to the degree of fracturation at Séchilienne. Finally, the low Na* concentration in the S12 outflow (Fig. 3) can be attributed to the fact that it mainly drains the carbonate cover. The most plausible explanation for the non-zero Na* concentration in S12 is the release of Na from silicate material disseminated in the carbonate rocks, and/or to anthropogenic inputs.

5.1.3 Identifying sources to solutes in the springs of the Séchilienne massif

In the following we use dissolved elemental and isotopic ratios to quantitatively constrain the contribution of various rock sources (silicates, carbonates, and gypsum) for solutes in the Séchilienne springs. As shown above, strong contrasts exist in ^{87}Sr/^{86}Sr ratios between the sedimentary carbonate cover and the crystalline rocks of the basement. The isotopic ratio of dissolved Sr released by water-rock interaction reflects that of the minerals undergoing dissolution and is not affected by the reincorporation of Sr in secondary minerals (*e.g.* Negrel et al. 1993). Sr isotopes can thus be used to trace the provenance of dissolved Sr, and by extension of the different cations, in the waters of Séchilienne. By contrast, elemental ratios such as Ca/Sr and Mg/Sr may be affected by the precipitation of secondary minerals and in particular by the formation of secondary carbonates (Bickle et al., 2015) and should be used more carefully to identify the provenance of cations.

A series of plots using ^{87}Sr/^{86}Sr as a common Y-axis are shown in Fig. 4. In ^{87}Sr/^{86}Sr *vs*. Ca/Sr or Na/Sr plots (Fig. 4a and 4b) conservative mixing between reservoirs is indicated by straight lines joining the end members. In this set of figures, the Ca/Sr ratios for the carbonate, silicate, and evaporite end members are taken from Négrel et al. (1993) and Gaillardet et al. (1997). The corresponding Sr isotopic ratios are those measured in the rock samples from the Séchilienne massif (Table 3).

The position of the data points corresponding to springs S13, S15, S18, S20, and S21 (MSZ group) in Fig. 4a and 4b shows that their relatively low Sr isotopic composition cannot only be derived from the dissolution of carbonates. Another unradiogenic end member with low Ca/Sr and Na/Sr ratios needs to be invoked. As indicated by Fig. 4c this end member is enriched in sulfate as shown by its high SO$_4$/Na ratio. Although gypsum outcrops are not visible at Séchilienne, gypsum is known to exist in the local Triassic formations present in the upper part of the slope as indicated by the regional geological map (Fig.1). More generally, the presence of gypsum is well documented in the Triassic strata of the the "external Alps" where it plays a major role in large-scale deformation and thrusting (Barféty et al. 1972). The occurrence of gypsum and carbonate dissolution inferred from the chemistry of the Séchilienne springs indicates that the Sabot Fault, which lies at the North-East of the MSZ outflows (Barféty et al. 1972), plays a major role in draining aquifers hosted by sedimentary rocks to the MSZ and BSZ outflows. The Sr and S isotope composition of Triassic seawater (between 0.7075 and 0.708 and 15±3 ‰, respectively; Burke et al. 1982, Fanlo and Aroya 1998, Kampschutte and Strauss 2004) and the typical Ca/Sr ratio of waters draining gypsum (Gaillardet et al., 1997; Meybeck et al., 1986) are consistent with the contribution of gypsum dissolution.

Fig. 4 also shows first that the S12 spring, reported by Vallet et al. (2015a) to be supplied by rapid flowpaths through the sedimentary cover, in addition to being solute-poor compared to springs of the MSZ group, is not influenced by gypsum

dissolution despite its geographical position on the sedimentary part of the slope. The relatively high Na/Sr ratios observed in the S12 spring is probably due to anthropogenic influence, as revealed by the high nitrate concentrations measured in this spring (section 5.1.1 and Fig. S8c).

By contrast, $^{87}Sr/^{86}Sr$ and chemical ratios of waters from the UZ outflows (G1, G2) are clearly influenced by a silicate end member. However, their Sr isotopic signature is lower than those of the local micaschist, indicating the additional contribution of Sr from a carbonate and / or evaporitic source to the G1 and G2 spring (Fig. 4a). The $^{87}Sr/^{86}Sr$ ratios of waters of the S10 outflow also exhibit intermediate values between the silicate and carbonate-gypsum mixing line, but with $^{87}Sr/^{86}Sr$ ratio lower than those of the UZ outflows, supporting the idea that water-silicate interaction in the BSZ are less intense than in the UZ. These inferences based on Sr isotopes are in full agreement with those made above based on Na* concentrations and can be interpreted as reflecting the lesser degree of fracturation of the stable zone compared to the unstable zone. Fig. 4c and Fig. 4d show that the higher $^{87}Sr/^{86}Sr$ ratios observed in springs of the UZ (G1, G2), and to a lesser extent of the BSZ (S10) are associated with sulfate enrichment. However, unlike for samples of the MSZ (S13-S21), dissolved sulfate in UZ and BSZ samples has a relatively low S isotope composition (Fig. 4d). This observation is compatible with a significant influence of sulfide oxidation, despite the very wide range of $\delta^{34}S$ values measured in the bedrock micaschists (between -13,14‰ and 17,77‰, average -0,10‰, S.D: 10,05; Table 2).

The presence of pyrite has been reported in the unstable zone of Séchilienne (Bertrand et al. 2014, Vallet et al. 2015a). The concomitant increase in SO_4^{2-} and radiogenic Sr (Fig. 4c), combined with the decrease in $\delta^{34}S$ (Fig. 4d) suggests a coupling in the unstable zone between sulfide oxidation and silicate weathering. Indeed, the oxidative weathering of pyrite, possibly by O_2 or water, leads to the release of sulfate to waters (e.g. Spence and Telmer, 2005):

$$2FeS_2 + \frac{15}{2}O_2 + 7H_2O \rightarrow 2Fe(OH)_3 + 4H_2SO_4 \tag{2}$$

$$FeS_2 + 14Fe^{3+} + 8H_2O \rightarrow 15Fe^{2+} + 2SO_4^{2-} + 16H^+ \tag{3}$$

The oxidation of sulfide to intermediate sulfur species or to sulfate appears to produce only small isotope effects (Fry et al., 1986, 1988; Zerkle et al., 2009; Balci et al., 2012). The significance of these reactions in the unstable zone of Séchilienne can be related to the role of fracturation and grain comminution in favoring the contact between water, air, and minerals, which is the rate-limiting factor for a fast chemical reaction such as pyrite oxidation.

Altogether, our analyses shows that the composition of the water outflows from the Séchilienne site can be interpreted by a variable contribution of waters having interacted with micaschists and sedimentary rocks, and by a dual origin (sulfide oxidation vs. gypsum dissolution) of sulfate ions. The chemical and isotopic characteristics of the MSZ and UZ waters show that these waters have percolated through the sedimentary cover before reaching their outlet in the massif through the Sabot fault.
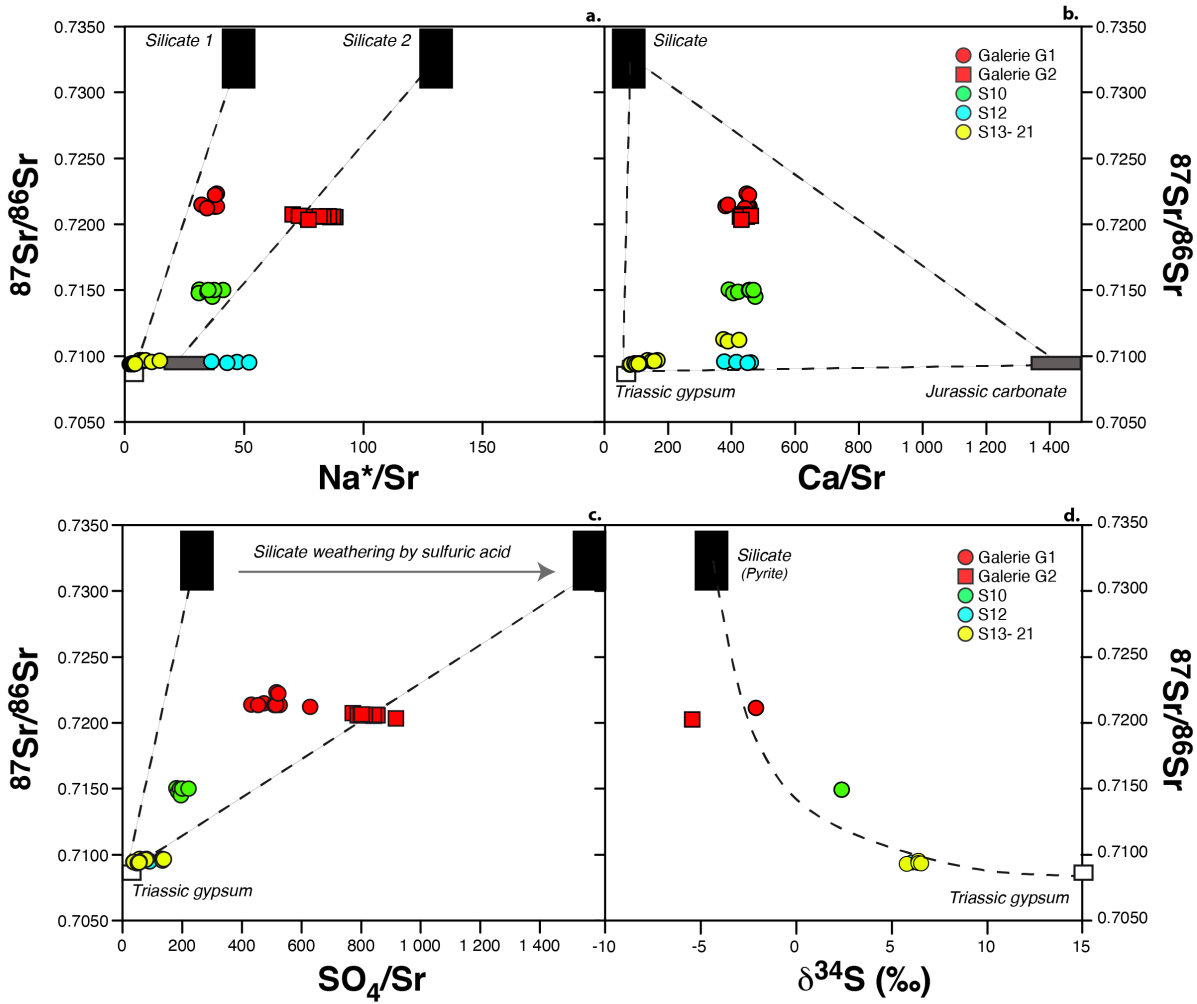
Figure 4: Sr isotopic composition of the different groups of water outflows from the Séchilienne massif as a function of Sr-normalized ratios (a, b and c) and S isotopic composition (d). Mixing end members are discussed in the text. Straight lines indicate a mixing process in Fig. 4a, 4b and 4c. In Fig. 4d, the dashed line is a mixing hyperbola calculated based on the composition of the end members (^{87}Sr/^{86}Sr, δ^{34}S, and SO$_4$/Sr ratios of the silicate and carbonate end members).

5.1.4 Quantitative apportionment

Spring dissolved Sr isotopes and major element chemistry make it possible to estimate the relative contribution of each identified end member to the different cations. The details of these calculations and results are given in supplementary materials. Following the above discussion, mixing equations can be written for the conservative trace element Sr:

$$\left(\frac{^{87}Sr}{^{86}Sr}\right)_{mix} = X_{sil}^{Sr} \cdot \left(\frac{^{87}Sr}{^{86}Sr}\right)_{sil} + X_{carb}^{Sr} \cdot \left(\frac{^{87}Sr}{^{86}Sr}\right)_{carb} + X_{gyps}^{Sr} \cdot \left(\frac{^{87}Sr}{^{86}Sr}\right)_{gyps} \tag{4}$$

$$\left(\frac{Na}{Sr}\right)_{mix} = X_{sil}^{Sr} \cdot \left(\frac{Na}{Sr}\right)_{sil} + X_{carb}^{Sr} \cdot \left(\frac{Na}{Sr}\right)_{carb} + X_{gyps}^{Sr} \cdot \left(\frac{Na}{Sr}\right)_{gyps} \tag{5}$$

$$1 = X_{sil}^{Sr} + X_{carb}^{Sr} + X_{gyps}^{Sr} \tag{6}$$

Where the subscripts *mix*, *sil*, *carb*, and *gyps* denote the mixture (water), the silicate, carbonate, and gypsum end members respectively. Proportions of Sr derived from each of those end members *i* are denoted X_i^{Sr}. All ratios are corrected from atmospheric and salt inputs according to the above method. Because the carbonate and gypsum end member add relatively few Na compared to Na* (Na from silicates), equation 5 simplifies into:

$$\left(\frac{Na}{Sr}\right)_{mix} = X_{sil}^{Sr} \cdot \left(\frac{Na}{Sr}\right)_{sil} \quad\quad\quad (7)$$

This assumption is supported by the positions of the different springs in Fig. 4a, which indicates that the low-$^{87}Sr/^{86}Sr$ component of the springs - encompassing both carbonate and gypsum weathering - has a negligible Na content. The proportions of Sr in the different mixing reservoirs can then be estimated and the contribution of each of these end members to the load of the dissolved major species SO_4^{2-} and Mg^{2+} then calculated following:

$$X_i^E = X_i^{Sr} \left(\frac{E}{Sr}\right)_i / \left(\frac{E}{Sr}\right)_{spring} \quad\quad\quad (8)$$

with i = sil, $carb$, or gyp, and E = SO_4, or Mg (corrected from rain inputs). Full discussion is given in supplementary materials (section 3) on the choice of the $(Na/Sr)_{sil}$ (eq. 7) and more generally of the $(E/Sr)_i$ ratios (eq. 8), based on regression of the spring hydrochemical data and independent constraints from our geochemical analyses of the rock samples.

In carbonate-rich contexts like that of Séchilienne, dissolved Ca^{2+} concentrations can be affected by precipitation of secondary carbonates which tend to scavenge significant amounts of dissolved Ca relative to Mg and Sr (Bickle et al., 2015). For this reason, in principle eq. 8 cannot be applied for E = Ca and i = $carb$. The relatively high Mg/Ca ratios (around 0.9 mol/mol in springs G1, G2, and S10; and 0.2-0.4 mol/mol in springs S10 to S21; Table 3) and Sr/Ca ratios (around 2 mmol/mol in springs G1, G2, S10, S12, and S18; and above 6 mmol/mol for springs S13, S15, S20, and S21) compared to the estimated Mg/Ca and Sr/Ca ratios of the calcite end member at Séchilienne (below 0.1 mol/mol and 1 mmol/mol, respectively) determined from our geochemical analyses of rock samples (Table 1) are indeed suggestive of a significant role of secondary carbonate formation. We quantify the role of secondary carbonate formation using the method proposed by Bickle et al. (2015), which is based on the comparison in the Sr-Ca-Mg-Na compositional space between the measurements made in springs and the prediction from conservative mixing between the rock end members (supplementary materials; section 3). In this analysis we contend that secondary carbonate formation affects waters containing solutes derived from the three rock end members identified for the Séchilienne springs (silicates, carbonates, and gypsum) after they mix. We estimate that along the water flowpath secondary carbonate formation scavenges around 60% of the Ca initially released to solution by the combined dissolution of silicates, carbonates, and gypsum for springs G1, G2, and S10, whereas the effect of secondary carbonate precipitation is negligible for the other springs (supplementary materials; section 3). These results highlight the potential role of lithological diversity, a characteristic of the bedrock material drained by springs G1, G2, and S10 in the UZ and BSZ (compared to other springs mostly influenced by the carbonate cover), in promoting secondary carbonate formation through mixing of compositionally different waters.

Another challenge in using eq. 8 at Séchilienne is the fact that both calcite and dolomite are reported to occur as carbonate minerals at Séchilienne - as confirmed by our own chemical analyses of rock samples (Tab. 1). Therefore, we take into account the presence of dolomite in our quantitative source apportionment, in particular regarding the $(Mg/Sr)_{carb}$ ratio used in eq. (8) (supplementary materials; section 3). Based on arguments linked to the extent of secondary carbonate precipitation needed to explain the spring data (see above), we estimate that the contribution of dolomite dissolution to the overall Ca released by carbonate weathering at Séchilienne is about 10 to 20% (supplementary materials).

In order to quantify the uncertainty associated to our mixing model, a Monte Carlo approach was used with 10,000 simulations. Results are given in Tab. S2 (tables available in supplementary materials) and represented in Fig. 5 as a stacked bar plot. In the following text, results on mixing proportions X_i^E are reported as $D_{50}{}^{+D_{84}}_{-D_{16}}$ (D_n is the nth percentile of the output distribution over the 10,000 simulations; D_{50} is thus the median).

Carbonate dissolution appears as the major contributor to dissolved Ca, and to about half of dissolved Mg in all the springs sampled on the different parts of the studied zone (UZ, BSZ, MSZ), making this process a major supplier of cationic charges

to waters at Séchilienne (Tab. S2; Fig. 5). In the most active part of the landslide (G1, G2), despite the silicate-dominated lithology, carbonate contribution is significant (about 40%), indicating the waters percolating though the unstable zone acquired part of their chemical and isotopic composition from above the hillslope. Calculations of the proportions of sulfate derived from the different end members show a minor but non negligible contribution of gypsum dissolution (reaching 88% of the total sulfate in spring S15) and a very clear contribution of pyrite oxidative weathering particularly important in the fractured zone. In the G1-G2-S10 group of springs, most of the anionic charge (> 80%) is provided by the oxidative weathering of pyrite. Springs from the BSZ exhibit a lower proportion from silicate end member with a median of $0.48_{0.24}^{0.76}$ against $0.61_{0.38}^{0.84}$, $0.56_{0.31}^{0.81}$ for G1 and G2 (UZ), respectively. This contrast can be attributed to the unstable context of G1 and G2 compared to that of the stable part of the slope at the BSZ outflow.

Gypsum dissolution is a major process at some sites (with fraction of SO_4 from gypsum ranging between $0.57_{0.43}^{0.79}$ and $0.88_{0.80}^{0.97}$ in waters of the MSZ S13-S21, for example), but nowhere does this process dominates the overall solute production (Fig. 5). Therefore, and although significant uncertainty exists regarding the S isotope composition of the pyrite endmember, S isotope data lend support to our inference from the mixing model that waters are derived essentially from pyrite oxidation in the unstable zone, and from gypsum dissolution the MSZ waters (S13, S15, S18, S20, S21). The relative contribution of carbonates is also significant in MSZ waters with proportions ranging from $0.32_{0.09}^{0.58}$ for S18 to $0.33_{0.13}^{0.56}$ for S15.

Based on results of the mixing model, we can estimate a value for $\delta^{34}S$ of the pyrite endmember. Indeed, a significant linear negative relationship ($R^2 = 0.8$) exists between the $\delta^{34}S$ measured in springs across the Séchilienne massif and the modal estimates of their X_{sil}^{SO4} (Fig. S12; supplementary materials). The intercept of this relationship at $X_{sil}^{SO4} = 1$ (equivalently at $X_{gyp}^{SO4} = 0$) gives an estimate for $\delta^{34}S_{sulfur}$ of -3.1‰. Such estimates are consistent with the range of measurements of solid sulfur reported in this study (ranging between -13.1‰ to 17.8‰) and reflect an average value of the S isotope composition of sulfides for the Séchilienne unstable zone.
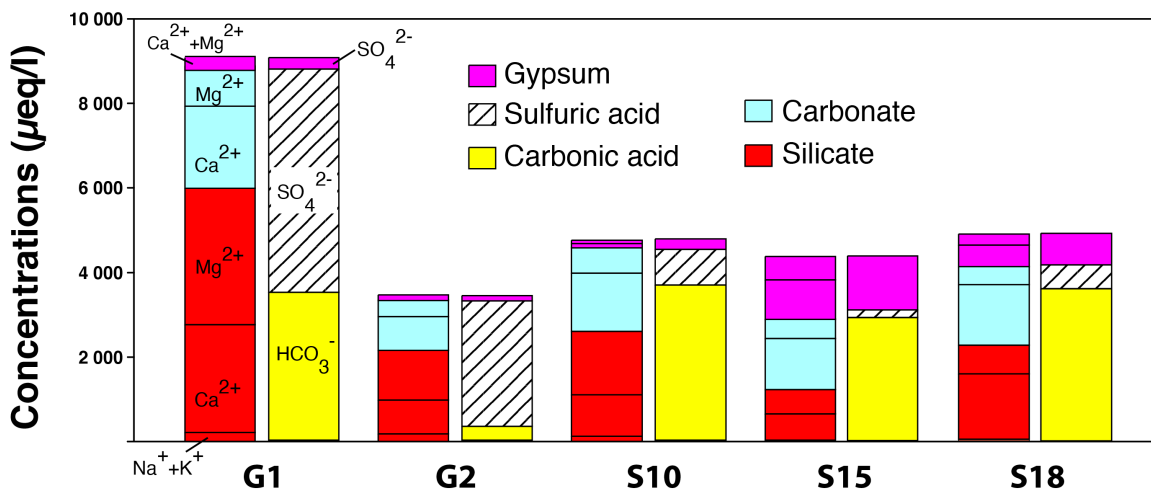
Figure 5: Concentration (in charge equivalents) calculated for major dissolved species and for each end member from the mixing model presented in the text and in the supplementary materials (Table S2). Silicates contribute for Na+K+Ca+Mg (Na+K not indicated), carbonates for Ca+Mg, gypsum dissolution for Ca+Mg (not distinguished). Note that ultimately the hydrogenocarbonate ion originates from respiration in soils. Sulfuric acid is generated by the oxidation of sulfide minerals, a process that occurs preferentially in the fractured zone. Relative contributions of different end members were obtained by solving a set of mixing equations using a Monte Carlo approach (section 5.1.3). Note that the relative contribution of each rock end member to the Ca^{2+} load here refers to that calculated for the Ca "initially" released into solution, that is before secondary carbonate precipitation (supplementary materials).

5.2 Implications for hydrogeological processes at the Séchilienne site

495 Water plays an important role in the dynamics of slope instabilities, first as a physical (hydrogeological) agent that can lead to aggravation of the instability. Secondly, water is a geochemical agent, which weathers rocks and makes them less cohesive (Rutqvist and Stephansson, 2003; Binet, 2006; Cappa et al., 2004). These two categories of processes interact with each other in time as weathering leads to modifications in subsurface permeability and porosity, and thus in water flowpaths through the massif (Gu et al. 2020). Hydrological triggering is the most usual mechanism of initiation and reactivation of

500 landslides but water flows in the subsurface have also been shown to have a major impact on the destabilization of a slope (de Montety et al. 2007; Guglielmi et al. 2002, Vallet et al. 2015b). However, landslides constitute very heterogeneous media due to their intense fracturation, which makes hydrogeological investigation complicated. The use of hydrochemistry and isotopic investigation can provide new insight to classical investigation. For example, groundwater dissolved ^{87}Sr/^{86}Sr ratios have proven to be useful in determining the sources of solutes in natural waters (Négrel and Deschamps, 1996, Négrel

505 et al., 2001, Dotsika et al., 2010), investigating mineral weathering reactions (Brass, 1975; Åberg et al., 1989; Bullen et al., 1996; Clow and Drever, 1996; Bullen and Kendall, 1998), and identifying mixing processes involving groundwaters of different sources (Woods et al., 2000; Frost and Toner, 2004; Singleton et al., 2006) also inside an unstable context (Deiana et al., 2018). Values of groundwater dissolved δ^{34}S-SO$_4^{2-}$ have also been used in aquifer studies to identify sulfate sources (Moncaster et al., 2000; Cortecci et al., 2002; Gammons et al., 2013). In particular, the Séchilienne hydrogeological model

510 proposed by Vallet et al. (2015a) use sulfates as a tracer of waters flowing through the instability with the assumption that all SO$_4^{2-}$ measured in groundwaters is sourced from pyrite oxidation. High sulfate concentrations in MSZ waters were indeed inferred by Vallet et al. (2015a) to be derived from a mixture of 30% of waters from the UZ (drained through the micro-fissured matrix) and 70% from the sedimentary cover (drained through both micro-fissured matrix and larger fractures), thereby establishing a hydraulic connection between the UZ and the MSZ waters (Fig. 1c).

515 Results from the present study partly support the hydrogeological model established by Vallet et al. (2015a) but allow us to refine this model through the identification of the contribution of another, unexpected end member corresponding to the dissolution of gypsum with a remote origin. Based on the local geological map (Barféty et al. 1972) gyspum occurrence has been reported but outside of the study zone, upstream along the Sabot fault which lies at the North-East of the MSZ outflows. As the fault is a major flowpath (Lajaunie et al., 2019), draining aquifers hosted by the sedimentary cover to the

520 MSZ outflows, it contributes to the enrichment in SO$_4^{2-}$ of those waters (Fig. 6). Our study therefore indicates a significant evaporitic origin for the sulfates in the MSZ waters, challenging the interpretation of Vallet et al. (2015a) of a hydrogeological connection between waters of the unstable and stable zones. Sulfate in outflows draining the UZ and BSZ is not strongly sourced from evaporites, but the part of those sulfates with evaporitic origin can be explained by a contribution of water flows through the Sabot fault towards the sedimentary cover and the basement formations (Fig. 6).

525 In addition, the systematic differences in elemental concentrations observed between the UZ and BSZ outflows (Tab. 3) can be linked to the structure of the slope and water flowpaths in the subsurface. Indeed, the S10 outflow drains a stable area (BSZ) just above the lowly-weathered, only slightly fractured basement. By contrast, the G1 and G2 outflows drain the unstable part of the slope (UZ), where the basement is highly fractured. This leads in turn to a stronger weathering degree of rocks and minerals there, and in particular of pyrite which is a major contributor to dissolved sulfate in the G1 and G2

530 outflows - more so than in the S10 outflow (stable and lowly weathered) characterized by lower sulfate contents.

Improving numerical and predictive models requires the incorporation of hydrological processes such as the dynamics of water circulation within a slope (directly dependent on fracturation, volumes of water involved, etc.). This study shows that isotopic proxies such as Sr and S isotopes (^{87}Sr/^{86}Sr, δ^{34}S) coupled to water chemistry can be a very powerful tool to constrain groundwater origin and flowpaths in landslides and can substitute to tracer surveys, and constitute an alternative

535 for hydrogeological investigations in logistically-challenging field environments such as unstable slopes.
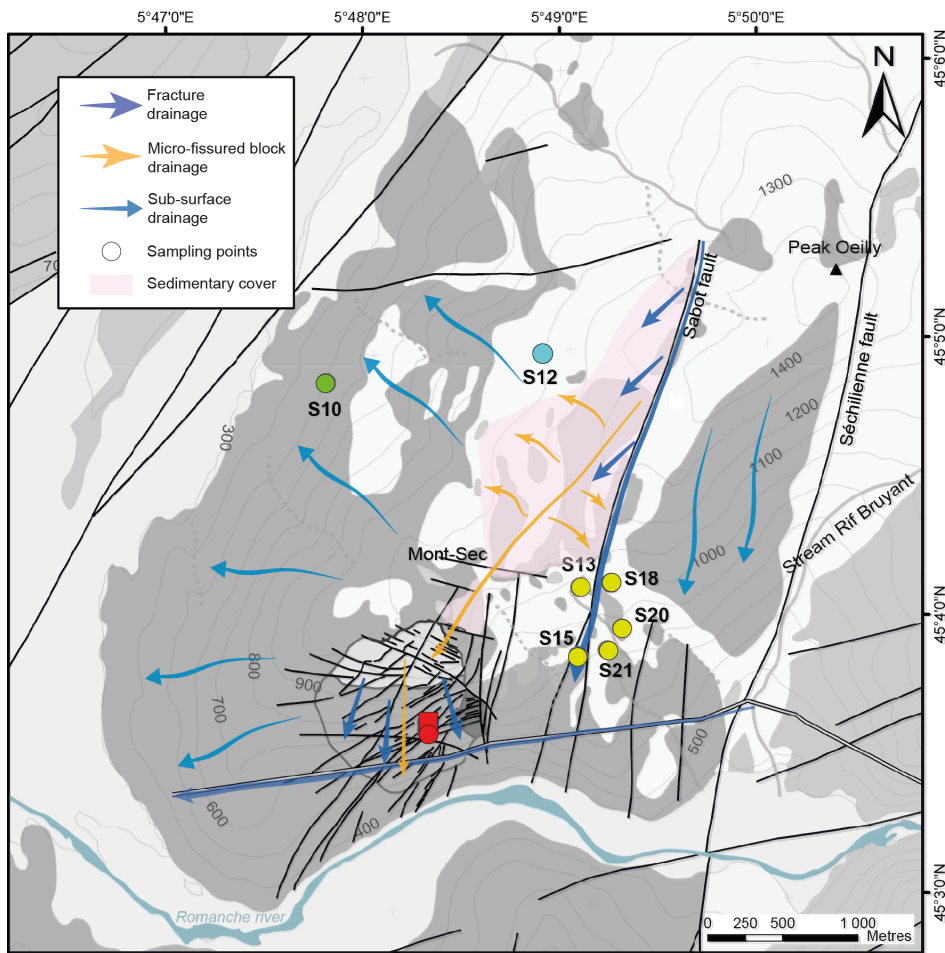
Figure 6: Sketch of the Séchilienne groundwater conceptual model, modified after Vallet et al., (2015).

5.3 Role of landslides on silicate weathering and CO₂ consumption

Recent studies have shown the importance of pyrite oxidation, sulfuric acid production, and associated chemical weathering in active landslides (Emberson et al. 2015, Emberson et al. 2016). The novelty of the present study is the use of waters sampled within an active, slow landslide, rather than percolation waters sampled at the base of the colluvium of recent landslides, of river waters draining landslide-affected watersheds. In the following paragraph we examine the potential implications of the present study of the Séchilienne landslide for the global carbon cycle.

Silicate weathering by carbonic acid consumes atmospheric CO₂ and, combined with the precipitation of carbonates in the ocean, is the mechanism that has allowed for the sequestration of atmospheric CO₂ and consequently lower the Earth's surface temperature on geological timescales (Berner and Berner 2012). Rock forming-minerals uplifted to the Earth surface react with oxygen, carbonic acid produced by soil respiration, and sulfuric acid produced by the oxidation of sulfide minerals. The following reactions describe how carbonic (equations 9 and 11) and sulfuric (equations 10 and 12) acids interact with silicate (here wollastonite CaSiO₃) and carbonate minerals, and lead to the production of alkalinity (here HCO₃⁻):

$$CaSiO_3 + 2CO_2 + H_2O \rightarrow SiO_2 + Ca^{2+} + 2HCO_3^- \qquad (9)$$
$$CaSiO_3 + H_2SO_4 \rightarrow SiO_2 + H_2O + Ca^{2+} + SO_4^{2-} \qquad (10)$$
$$CaCO_3 + CO_2 + H_2O \rightarrow Ca^{2+} + 2HCO_3^- \qquad (11)$$
$$2CaCO_3 + H_2SO_4 \rightarrow 2Ca^{2+} + 2HCO_3^- + SO_4^{2-} \qquad (12)$$

It is usually considered that when Ca^{2+} reaches the ocean, over a time period longer than 0.1 to 1 Myr, the precipitation of $CaCO_3$ releases CO_2 into the ocean-atmosphere system according to the reaction:

$$Ca^{2+} + 2HCO_3^- \leftrightarrow CaCO_3 + CO_2 + H_2O \tag{13}$$

The influence of the above reactions (equations 9-13) on atmospheric CO_2 partial pressure depends on the time scale considered (Torres et al., 2016). At short timescales (typically $< 10^5$ yrs), the chemistry of river discharge is able to influence the carbonate system in the ocean. Indeed, the delivery of alkalinity and Dissolved Inorganic Carbon (DIC) to the ocean to a ratio lower than that of the modern seawater ratio (Alk/DIC ~ 1) leads to increased dissolved CO_2 concentration, and consequently higher CO_2 content in the atmosphere through re-equilibration (Zeebe and Wolf-Gladrow, 2001). If the Alk/DIC ratio is higher than 1 but lower than 2, at time scales longer than that typical of carbonate precipitation in the ocean (10^5 to 10^6 yrs) but shorter than that of marine sulfate reduction to sulfide in sea bottom sediments (several 10^6 yrs), atmospheric CO_2 will increase because the precipitation of carbonates releases CO_2 to the ocean-atmosphere system that was not consumed on land by weathering reactions (combination of equations. 12 and 13). This mechanism should lead to global warming (Calmels et al., 2007) and has been invoked by Torres et al. (2014) for maintaining atmospheric CO_2 levels during the Himalayan orogeny, which otherwise should have led to a rapid atmospheric CO_2 depletion by enhanced silicate weathering. Finally, at timescales longer than that typical of sedimentary burial of sulfide in the ocean, only silicate weathering by carbonic acid leads to net C sequestration (Berner et Berner, 1996; Calmels et al. 2007).

However, our analysis demonstrates that at Séchilienne reaction (13) also occurs directly on the continent through the formation of secondary carbonates, favored by the addition of calcium and alkalinity derived from silicate weathering, which results in a "short cut" of the carbon cycle. This short-term CO_2 release has to be taken into account when evaluating the overall CO_2 effect of weathering reactions at Séchilienne, and more generally in lithologically complex weathering systems where secondary carbonate formation is likely to involve solutes produced by a variety of processes, and in particular by carbonate weathering by sulfuric acid.

To this aim, we use the stoichiometry of reactions (9) to (13), together with the results of our quantitative source apportionment (section 5.1.4) to calculate the impact of weathering reactions at Séchilienne on atmospheric CO_2 over two scales (convoluted spatially and temporally), referred to in the following as "on site" or "local" (*i.e.*, immediately when weathering processes take place in the unstable zone) and "long term" or "global" (i.e., taking into account marine carbonate precipitation in the ocean ensuing solute delivery to the ocean).

Fig. 7 shows that waters produced in the Unstable Zone of Séchilienne (G1 and G2) act as CO_2 sources on the "long term", whereas waters produced in the bedrock stable zone (S10) or the mixed stable zone (S15, S18) are CO_2 sinks or CO_2-neutral within uncertainty. Our study thus shows that instabilities such as the Séchilienne landslide can act as hotspots of long-term CO_2 release to the atmosphere depending on the types of mineral-fluid interactions and also on the flow paths followed by the water drained in the landslide. We suggest that chemical weathering in similar landslides throughout the Alps (i.e Clapière, Super Sauze, and Valabres in the French Alps, Rosone in Italy; Barla et Chiriotti, 1995; Follacci, 1999; Binet, 2006) have a similar impact on global biogeochemical cycles and climate. Although it is beyond the scope of the present study to quantify the CO_2 fluxes linked to weathering in the Séchilienne landslide - let alone to attempt an extrapolation of such local results to the scale of the Alpine range - our work clearly shows that silicate and carbonate weathering by sulfuric acid generated in landslide zones of active mountain ranges have a climatic impact though a complex set of entangled short-term and long-term effects. Furthermore, this impact contradicts the textbook view that silicate weathering in mountain ranges consumes CO_2 from the atmosphere and cool the global climate (Raymo, 1991; Hilton and West 2020), and motivates more detailed studies associating hydrogeological and mineralogical approaches to build a more realistic understanding of the impact of mountains on climate change.
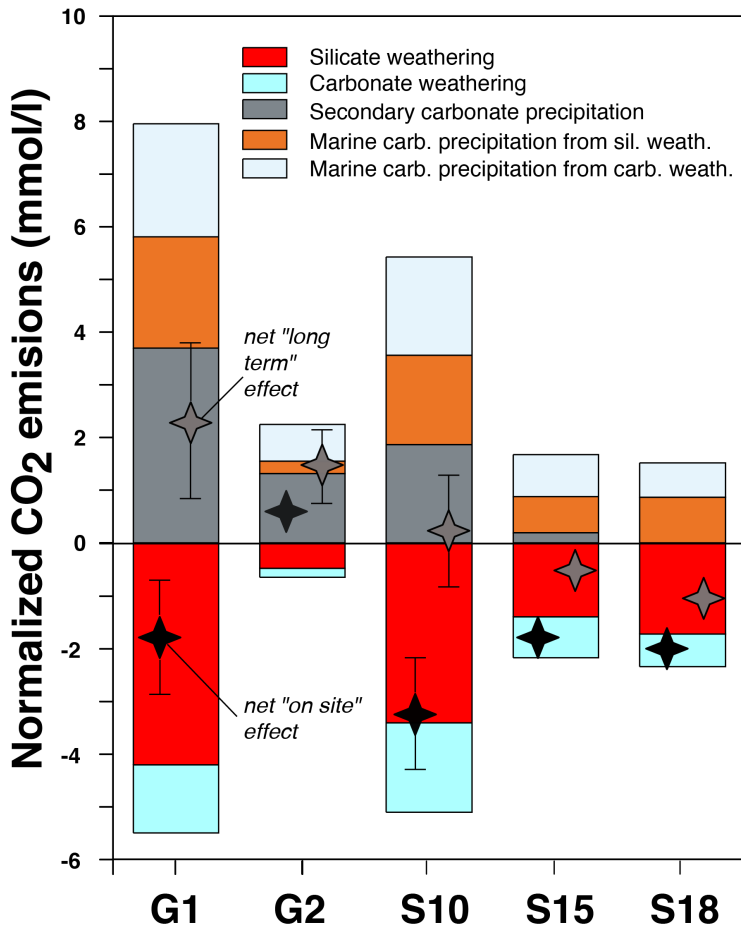
Figure 7: Evaluation of the effect of weathering processes at Séchilienne on atmospheric CO_2. The hydrochemistry of the springs G1 and G2 draining the instability ("Unstable Zone") show that the weathering results in long-term CO_2 production to the atmosphere because the cations are preferentially released in spring waters by the action of sulphuric acid and not carbonic acid from the soils (Table S3; supplementary materials). In the Bedrock Stable Zone (spring S10) and in the Mixed Stable Zone (springs S15 and S18), weathering processes act as CO_2 sinks or are CO_2-neutral within uncertainty. Secondary carbonate precipitation returns CO_2 to the atmosphere. In particular, in the spring G2 of the Unstable Zone, this process results in a net "on site" CO_2 release because it involves precipitation of Ca and alkalinity derived from carbonate weathering by sulfuric acid.

6. Conclusion

We use measurements of dissolved major element chemistry coupled to Sr and S isotopic ratios in spring waters of the Séchilienne active landslide site in order to identify the chemical processes at play in the subsurface of the landslide area. Among these tracers, strontium isotopes allow us to allocate cations to different sources, circumventing issues affecting elemental ratios related to the precipitation of secondary. Silicate, carbonate, and evaporite weathering all appear to contribute to the cation load of the Séchilienne waters. Scavenging of dissolved calcium by secondary carbonate formation is identified as a major process affecting solutes in the subsurface waters of the Séchilienne instability and favored by the mixing of different solution having interacted with a heterogeneous set of minerals. Sulfur isotopes bring a unique qualitative constraint on the origin of the sulfate ion, which is abundant in the Séchilienne groundwaters, showing the contribution of not only pyrite oxidation but also of gypsum dissolution.

The provenance of dissolved species at Séchilienne also reveals the complex water flow paths there. In particular, waters percolating through the landslide have acquired part of their hydrochemical characteristics far away from the unstable zone itself. For example, sulfur isotopes clearly indicate an unexpected contribution from Triassic sedimentary gypsum

625 dissolution, that can only occur in the sedimentary layers capping the upper part of the massif and pointing out the importance of water drainage by a major fault of the massif.

The comparison between the stable and unstable parts of the site suggests that silicate weathering is enhanced in the fractured, unstable zone, where the landslide is active. Sulfur isotopes indicate that the production of acidity by the oxidation of magmatic sulfides enhances rock alteration in the unstable zone, this leads us to suggest the following feedback. By
630 favoring the penetration of oxic waters and allowing contact with silicate minerals, fracturation and grain comminution controls the oxidation of pyrite that in turn rapidly generates sulfuric acid. The weathering of silicate minerals by sulfuric acid weakens the rock structure what in turn favors fracturation in response to the gravitational stress. For example, Fletcher et al. (2006) and Behrens et al. (2015) have shown that opening of porosity at the rock-soil interface in soil profiles can be initiated by oxidation of Fe(II) minerals inducing a positive volume budget leading to the production of micro-cracks,
635 inducing further weathering, at the origin of the opening of fractures, provided that enough carbonate and pyrite is present in the bedrock. At a larger scale, the feedback we propose here exemplifies a similar process of coupling between physical and chemical processes sustaining mass wasting in mountain ranges.

Finally, we demonstrate that the Séchilienne landslide is a hotspot of CO_2 release to the atmosphere over the long term. Although it remains difficult to upscale the results of the present study to the entire Alpine range, or to a global scale,
640 landslides developed on sulfide-hosting sedimentary rocks appear to have a climatic impact opposite to the conventional view that rock weathering in mountains ranges consumes CO_2 from the atmosphere, and thus contributes to global cooling. In addition, our study shows a strong control of weathering processes and rates by local hydrogeological features, such as the complexity of flow paths setting the chemistry of the groundwaters within the unstable zone. More work is needed to assess the importance of landslides as hotspots of chemical alteration and geological CO_2 emissions, in particular to investigate
645 their hydrological and hydrochemical response to weather and climate change. More generally, landslides epitomize the coupling between landscape evolution, tectonics and climate-weather. For this reason - as well as that of their societal impact in terms of natural hazard - monitoring landslides over a range of time scales and frequency should become a priority.

Team list

650   Pierre Nevers

Julien Bouchez

Jérôme Gaillardet

Thomazo Christophe

Charpentier Delphine

655   Laëticia Faure

Catherine Bertrand

Author contribution

Pierre Nevers measured the Sr isotopic ratios, worked on the interpretation and wrote text. Julien Bouchez and Jérôme Gaillardet helped with the isotopic measurements, in the inversion calculations and in writing text. Christophe Thomazo
660   measured the sulfur isotopic ratios. Delphine Charpentier worked on XRD and mineralogic analyses presented in supplementary materials. Laëticia Faure helped with the rock sample leaching procedure and Sr isotope measurements. Catherine Bertrand organized the sampling strategy and is in charge of the Séchilienne Observatory (SNO OMIV) and helped in writing text.

Competing interests

665   The authors declare that they have no conflict of interest.

Acknowledgments

Part of this work was supported by IPGP multidisciplinary program PARI and by Region île-de-France SESAME Grant no. 12015908. Caroline Gorge, Christophe Loup and Caroline Amiot are acknowledged for analytical support, and Vanessa
670   Stefani is acknowledged for support on the field. The authors warmly thank: the PEA²t platform (Chrono environment, University of Bourgogne Franche-Comté, UMR CNRS 6249, France), which manages and maintains the analytical equipment used in this study; and OMIV and OSU Theta for supporting the project through financial contributions (SRO_2015).

References

675   Barféty, J., Bordet, P., Carme, F., Debelmas, J., Meloux, M., Montjuvent, G., Sarrot Reynauld, J.: Carte géologique détaillée de la France (1/50000) n°797 Vizille. Editions du BRGM, p. 38, 1972

Barla, G. et Chiriotti, E., 1995. Insights into the behaviours of the large deep seat gravitational slope deformation of Rosone, in the Piemont region (Italy). Felsbau, 13:
680   425-432

Baudement, C., Bertrand, C., Guglielmi, Y., Viseur, S., Vallet, A., & Cappa, F.: Quantification de la dégradation mécanique et chimique d'un versant instable : approche géologique, hydromécanique et hydrochimique Etude du versant instable de Séchilienne, Isère (38). 1–6, 2013

685

Behrens R., Bouchez J., Schuessler J. A., Dultz S., Hewawasam T. and von Blanckenburg F. (2015) Mineralogical transformations set slow weathering rates in low-porosity metamorphic bedrock on mountain slopes in a tropical climate. Chem. Geol. 411, 283–298, https://doi.org/ 10.1016/j.chemgeo.2015.07.008, 2015

690   Berner,K.E. and Berner,R.A.: Global Environment: Water, Air and Geochemical Cycles,Princeton Univ. Press, 369–382, 2012

Bertrand, C., Vallet, A., Mudry, J.,: Hydrochemical Approach of Mechanical Degradation of the Séchilienne Unstable Slope, in Engineering Geology for Society and Territory – Volume 2, edited by: Lollino, G., Giordan, Crosta, G. B., Corominas, J.,
695   Azzam, R., Wasowski, J., Sciarra, N., Springer International Publishing Switzerland, chapter: 383, https://doi.org/10.1007/978-3-319-09057-3_383, 2015

Bickle, M. J., Tipper, E. T., Galy, A., Chapman, H., and Harris, N.: On Discrimination Between Carbonate and Silicate Inputs to Himalayan Rivers, Am. J. Sci., 315, 120–166, https://doi.org/10.2475/02.2015.02, 2015
700

Binet, S., Spadini, L., Bertrand, C., Guglielmi, Y., Mudry, J., and Scavia, C.: Variability of the groundwater sulfate concentration in fractured rock slopes: a tool to identify active unstable areas, Hydrol. Earth Syst. Sci., 13, 2315–2327, https://doi.org/10.5194/hess-13-2315-2009, 2009

705   Blattmann T. M., Wang, S. L., Lupker, M., Märki, L., Haghipour, N., Wacker, L., Chung, L. H., Bernasconi, S. M, Plötze, M., Eglinton, T. I.: Sulphuric acid-mediated weathering on Taiwan buffers geological atmospheric carbon sinks, Sci Rep, 2945, https://doi.org/10.1038/s41598-019-39272-5, 2019
Brass, G. W.: The effect of weathering on the distribution of strontium isotopes in weathering profiles. Geochimica et Cosmochimica Acta, 39, 1647–1653, https://doi.org/10.1016/0016-7037(75)90086-1, 1975
710

Bullen, T. D., Krabbenhoft, D. P., Kendall, C.: Kinetic and mineralogic controls on the evolution of groundwater chemistry and 87Sr/86Sr in a sandy silicate aquifer, northern Wisconsin, USA. Geochimica et Cosmochimica Acta, 60(10), 1807–1821, https://doi.org/10.1016/0016-7037(96)00052-X, 1996

715   Bullen, T. D. and Kendall, C.: Tracing of Weathering Reactions and Water Flowpaths: A Multi-isotope Approach, in: Isotope Tracers in Catchment Hydrology, edited by Kendall, C., McDonnell, J. J, Elsevier Science B.V., Amsterdam, pp. 611-646, https://doi.org/10.1016/B978-0-444-81546-0.50025-2, 1998

Burke, W.H., Denison, R.E., Hetherington, E.A., Koepnick, R.B., Nelson, H.F. and Otto, J.B.: Variation of seawater
720   87Sr/86Sr throughout Phanerozoic time. Geology 10: 516-519., https://doi.org/10.1130/0091-7613(1982)10<516:VOSSTP>2.0.CO;2, 1982

Calmels, D., Gaillardet, J., Brenot, A., & France-Lanord, C.: Sustained sulfide oxidation by physical erosion processes in the Mackenzie River basin: Climatic perspectives, Geology, 35(11), 1003–1006, https://doi.org/10.1130/G24132A.1, 2007
725

Canfield, D. E., Raiswell, R., Westrich, J. T., Reaves, C. M., Berner, R. A.: the use of chromium reduction in the analysis of reduced inorganic sulfur in sediments and shales, Chemical Geology, 54(1-2), 149–155, https://doi.org/10.1016/0009-2541(86)90078-1, 1986

730 Cappa, F., Guglielmi, Y., Soukatchoff, V., Mudry, J., Bertrand, C., Charmoille, A.: Hydromechanical modeling of a large moving rock slope inferred from slope levelling coupled to spring long-term hydrochemical monitoring: example of the La Clapière landslide (Southern Alps, France), Journal of Hydrology, 291(1–2), 67–90, https://doi.org/10.1016/J.JHYDROL.2003.12.013, 2004

735 Cervi, F., Ronchetti, F., Martinelli, G., Bogaard, T. A., and Corsini, A.: Origin and assessment of deep groundwater inflow in the Ca' Lita landslide using hydrochemistry and in situ monitoring, Hydrol. Earth Syst. Sci., 16, 4205–4221, https://doi.org/10.5194/hess-16-4205-2012, 2012

Clow, D. W and Drever, J. I.: Weathering rates as a function of flow through an alpine soil, Chemical Geology, 132(1–4),
740 131–141, https://doi.org/10.1016/S0009-2541(96)00048-4, 1996

Cortecci, G., Dinelli, E., Bencini, A., Adorni-Braccesi, A., La Ruffa, G.: Natural and anthropogenic SO4 sources in the Arno river catchment, northern Tuscany, Italy: a chemical and isotopic reconnaissance, Applied Geochemistry, 17(2), 79–92, https://doi.org/10.1016/S0883-2927(01)00100-7, 2002
745

Deiana, M., Cervi, F., Pennisi, M., Mussi, M., Bertrand, C., Tazioli, A., Ronchetti, F.: Chemical and isotopic investigations (δ18O, δ2H, 3H, 87Sr/86Sr) to define groundwater processes occurring in a deep-seated landslide in flysch. Hydrogeology Journal, 26(8), 2669–2691, https://doi.org/10.1007/s10040-018-1807-1, 2018

750 Dotsika, E., Poutoukis, D., Kloppmann, W., Guerrot, C., Voutsa, D., Kouimtzis, T. H.: The use of O, H, B, Sr and S isotopes for tracing the origin of dissolved boron in groundwater in Central Macedonia, Greece. Applied Geochemistry, 25(11), 1783–1796. https://doi.org/10.1016/J.APGEOCHEM.2010.09.006, 2010

Dubois, L., Chanut, M.-A., Duranthon, J. P.: Amélioration continue des dispositifs d'auscultation et de surveillance integrés
755 dans le suivi du versant instable des Ruines de Séchilienne in : Géologues, 182, edited by : Editions du BRGM, 50–55, 2014

Emberson, R., Hovius, N., Galy, A. Marc, O.: Chemical weathering in active mountain belts controlled by stochastic bedrock landsliding, Nature Geoscience, 9, 42–45, https://doi.org/10.1038/ngeo2600, 2015

760 Emberson, R., Hovius, N., Galy, A., Marc, O.: Oxidation of sulfides and rapid weathering in recent landslides, Earth Surface Dynamics, 4(3), 727–742, https://doi.org/10.5194/esurf-4-727-2016, 2016b

Emberson, R., Galy, A., Hovius, N.: Weathering of Reactive Mineral Phases in Landslides Acts as a Source of Carbon Dioxide in Mountain Belts, Journal of Geophysical Research: Earth Surface, 123(10), 2695–2713.
765 https://doi.org/10.1029/2018JF004672, 2018

Fanlo, I. and Ayora, C.: The evolution of the Lorraine evaporitic basin: implications for the chemical and isotope composition of the Triassic ocean, Chemical Geology, vol. 146 n° 3-4, p. 135–154, https://doi.org/10.1016/S0009-25419800007-2, 1998

770

Fletcher, R. C., Buss, H. L., and Brantley, S. L.: A spheroidal weathering model coupling porewater chemistry to soil thicknesses during steady-state denudation, Earth Planet. Sci Lett., 244, 444-457, https://doi.org/10.1016/j.epsl.2006.01.055, 2006

Follacci, J.: Seize ans de surveillance du glissement de la Clapière (Alpes maritimes). 220, Rapport, Bulletin du Laboratoire

775   des Ponts et Chaussés. 35-51, 1999

Frost, C. D., Toner, R. N.: Strontium isotopic identification of water-rock interaction and ground water mixing, Ground Water, 42(3), 418–432, https://doi.org/10.1111/j.1745-6584.2004.tb02689.x, 2004

780   Gaillardet, J., Dupre, B., Allegre C. J., Négrel, P.: Chemical and physical denudation in the Amazon River Basin, Chemical Geology, vol. 142 n° 3–4, p. 141-173, https://doi.org/10.1016/S0009-2541(97)00074-0, 1997

Gaillardet, J., Dupre, B., Louvat, P., Allegre, C. J.: Global silicate weathering and CO2 consumption rates deduced from the chemistry of large rivers, Chemical Geology, 159, 3–30, https://doi.org/10.1016/S0009-2541(99)00031-5, 1999

785

Gammons, C. H., Brown, A., Poulson, S. R., Henderson, T. H.: Using stable isotopes (S, O) of sulfate to track local contamination of the Madison karst aquifer, Montana, from abandoned coal mine drainage, Applied Geochemistry, 31, 228–238, https://doi.org/10.1016/J.APGEOCHEM.2013.01.008, 2013

790   Gu, X., Rempe, D., Dietrich, W., West, A., Lin, T.C., Jin, L., Brantley, S.: Chemical reactions, porosity, and microfracturing in shale during weathering: The effect of erosion rate. Geochimica et Cosmochimica Acta. 269, 2019

Guglielmi, Y., Vengeon, J., Bertrand, C., Mudry, J., Follacci, J., Giraud, A.: Hydrogeochemistry: an investigation tool to evaluate infiltration into large moving rock masses (case study of La Clapière and Séchilienne alpine landslides), Bulletin of

795   Engineering Geology and the Environment, 61(4), 311–324. https://doi.org/10.1007/s10064-001-0144-z, 2002

Hajj, F., Poszwa, A., Bouchez, J., Guérold, F.: Radiogenic and "stable" strontium isotopes in provenance studies: A review and first results on archaeological wood from shipwrecks, Journal of Archaeological Science, 86, 24–49, https://doi.org/10.1016/j.jas.2017.09.005, 2017

800

Hilton, R.G. and West, A.J.: Mountains, erosion and the carbon cycle, Nature reviews earth & environment, 1 (6). pp. 284-299, https://doi.org/10.1038/s43017-020-0058-6, 2020

Kampschulte, A., Strauss, H.: The sulfur isotopic evolution of Phanerozoic seawater based on the analysis of structurally

805   substituted sulfate in carbonates, Chemical Geology, 204(3–4), 255–286, https://doi.org/10.1016/j.chemgeo.2003.11.013, 2004

Koepnick, R. B., Denison, R. E., Burke, W. H., Hetherington, E. A., Dahl, D. A.: Construction of the Triassic and Jurassic portion of the Phanerozoic curve of seawater 87Sr/86Sr, Chemical Geology: Isotope Geoscience Section, 80(4), 327–349, https://doi.org/10.1016/0168-9622(90)90014-4, 1990

Lajaunie, M., Gance, J., Nevers, P., Malet, J.-P., Bertrand, C., Garin, T., and Ferhat, G.: Structure of the Séchilienne unstable slope from large-scale 3d electrical tomography using a resistivity distributed automated system (r-das). Geophysical Journal International, https://doi.org/10.1093/gji/ggz259, 2019

Lasaga, A. C.: Chemical kinetics of water-rock interactions, Journal of Geophysical Research: Solid Earth, 89(B6), 4009–4025, https://doi.org/10.1029/jb089ib06p04009, 1984

Lerman, A., Wu, L., Mackenzie, F. T.: CO2 and H2SO4 consumption in weathering and material transport to the ocean, and their role in the global carbon balance, Marine Chemistry, 106(1-2 SPEC. ISS.), 326–350, https://doi.org/10.1016/j.marchem.2006.04.004, 2007

Le Roux, O., Jongmans, D., Kasperski, J., Schwartz, S., Potherat, P., Lebrouc, V., Meric, O.: Deep geophysical investigation of the large Séchilienne landslide (Western Alps, France) and calibration with geological data, Engineering Geology, 120(1–4), 18–3, https://doi.org/10.1016/J.ENGGEO.2011.03.004, 2011

Li, S. L., Calmels, D., Hana, G., Gaillardet, J., Liu, C. Q.: Sulfuric acid as an agent of carbonate weathering constrained by δ13CDIC: Examples from Southwest China, Earth and Planetary Science Letters, 270, 3–4, 30, 189-199, https://doi.org/10.1016/j.epsl.2008.02.039, 2008

Maréchal, J.-C., 1998. Les circulations d'eau dans les massifs cristallins alpins et leurs relations avec les ouvrages souterrains, Ecole Polytechnique Fédérale de Lausanne (EPFL), 1998

Meric, O., Garambois, S., Jongmans, D., Wathelet, M., Chatelain, J. L., Vengeon, J. M.: Application of geophysical methods for the investigation of the large gravitational mass movement of Séchilienne, France, Canadian Geotechnical Journal, 42(4), 1105–1115, https://doi.org/10.1139/t05-034, 2005

Meybeck Michel. Composition chimique des ruisseaux non pollués en France. Chemical composition of headwater streams in France. In: Sciences Géologiques, tome 39, n°1, pp. 3-77, https://doi.org/10.3406/sgeol.1986.1719, 1986

Meynadier, L., Gorge, C., Birck, J., Allègre, C.: Automated separation of Sr from natural water samples or carbonate rocks by high performance ion chromatography, Chemical Geology, 227(1–2), https://doi.org/10.1016/j.chemgeo.2005.05.012, 2006

Moncaster, S. J., Bottrell, S. H., Tellam, J. H., Lloyd, J. W., Konhauser, K. O.: Migration and attenuation of agrochemical pollutants: Insights from isotopic analysis of groundwater sulphate, Journal of Contaminant Hydrology, 43(2), 147–163, https://doi.org/10.1016/S0169-7722(99)00104-7, 2000

Montety, V. de, Marc, V., Emblanch, C., Malet, J.-P., Bertrand, C., Maquaire, O., Bogaard, T. A.: Identifying the origin of
850   groundwater and flow processes in complex landslides affecting black marls: insights from a hydrochemical survey, Earth
Surface Processes and Landforms, 32(1), 32–48, https://doi.org/10.1002/esp.1370, 2007

Montjuvent, G. and Winistorfer, J.: Glaciations quaternaires dans les Alpes franco-suisses et leur piedmont, in Géologie
Alpine, 56, 251–282, 1980
855

Mudry, J., & Etievant, K., 2007. Synthese hydrogéologique du versant instable des Ruines de Séchilienne (Unpublished
report), UMR Chrono-Environnement, University of Franche-Comté, Besançon, 2007

Négrel, P., Allègre, C. J., Dupré, B., Lewin, E.: Erosion sources determined by inversion of major and trace element ratios
860   and strontium isotopic ratios in river: The Congo Basin case, Earth and Planetary Science Letters, 120(1–2), 59–76,
https://doi.org/10.1016/0012-821X(93)90023-3, 1993

Négrel, P. and Deschamps, P.: Natural and anthropogenic budgets of a small watershed in the massif central (France):
Chemical and strontium isotopic characterization of water and sediments, Aquatic Geochemistry, 2(1), 1–27,
865   https://doi.org/10.1007/BF00240851, 1996

Négrel, P., Casanova, J., Aranyossy, J.-F.: Strontium isotope systematics used to decipher the origin of groundwaters
sampled from granitoids: the Vienne Case (France), Chemical Geology, 177(3–4), 287–308, https://doi.org/10.1016/S0009-
2541(00)00414-9, 2001
870

Oudin, L., Hervieu, F., Michel, C., Perrin, C., Andréassian, V., Anctil, F., and Loumagne, C.: Which potential
evapotranspiration input for a lumped rainfall–runoff model?: Part 2—towards a simple and efficient potential
evapotranspiration model for rainfall–runoff modelling, Journal of hydrology, 303(1-4):290–306, 2005

875   Raymo, M. E.: Geochemical evidence supporting T. C. Chamberlin's theory of glaciation, Geology, 19, 344–347,
https://doi.org/10.1130/0091-7613(1991)019<0344:GESTCC>2.3.CO;2, 1991

Raymo, M., Ruddiman, W.: Tectonic forcing of late Cenozoic climate, Nature, 359, 117–122,
https://doi.org/10.1038/359117a0, 1992
880

Russell, W. A. and Papanastassiou, D. A.: Calcium isotope fractionation in ion-exchange chromatography, Analytical
Chemistry, 50(8), 1151–1154, https://doi.org/10.1021/ac50030a036, 1978

Singleton, M. J., Maher, K., DePaolo, D. J., Conrad, M. E., Evan Dresel, P.: Dissolution rates and vadose zone drainage
885   from strontium isotope measurements of groundwater in the Pasco Basin, WA unconfined aquifer, Journal of Hydrology,
321(1–4), 39–58, https://doi.org/10.1016/J.JHYDROL.2005.07.044, 2006

Spence, J., Telmer, K.: The role of sulfur in chemical weathering and atmospheric CO2 fluxes: evidence from major ions,
δ13CDIC, and δ34S SO4 in rivers of the Canadian Cordillera, Geochimica Cosmochemica, 69, 5441–5458,
890   https://doi.org/10.1016/j.gca.2005.07.011,2005

Stallard, R. F. and Edmond, J. M.: Geochemistry of the Amazon: 2. The influence of geology and weathering environment on the dissolved load, Journal of Geophysical Research: Oceans, 88, 9671–9688, https://doi.org/10.1029/jc088ic14p09671, 1983

895

Torres, M. A., West, A. J., Li, G.: Sulphide oxidation and carbonate dissolution as a source of CO_2 over geological timescales, Nature, 507(7492), 346–349, https://doi.org/10.1038/nature13030, 2014

Torres, M. A., West, A. J., Clark, K. E., Paris, G., Bouchez, J., Ponton, C., Adkins, J. F.: The acid and alkalinity budgets of weathering in the Andes–Amazon system: Insights into the erosional control of global biogeochemical cycles. Earth and Planetary Science Letters, 450, 381–391, https://doi.org/10.1016/j.epsl.2016.06.012, 2016

Vallet, A. Mouvements de fluides et processus de déstabilisation des versants alpins : Apport de l'étude de l'instabilité de Séchilienne, Université de Franche-Comté, 2014

905

Vallet, A., Bertrand, C., Mudry, J., Bogaard, T., Fabbri, O., Baudement, C., Régent, B.: Contribution of time-related environmental tracing combined with tracer tests for characterization of a groundwater conceptual model: a case study at the Séchilienne landslide, western Alps (France), Hydrogeology Journal, 23(8), 1761–1779, https://doi.org/10.1007/s10040-015-1298-2, 2015a

910

Vallet, A., Charlier, J. B., Fabbri, O., Bertrand, C., Carry, N., Mudry, J.: Functioning and precipitation-displacement modelling of rainfall-induced deep-seated landslides subject to creep deformation, Landslides, 13, 653–670, https://doi.org/10.1007/s10346-015-0592-3, 2015b

915 Vengeon, J. M.: Déformation et rupture des versants en terrain métamorphique anisotrope : Apport de l' étude des Ruines de Séchilienne, Université Joseph-Fourier - Grenoble I, 1998

Vengeon, J.-M., Couturier, B., Antoine, P.: Déformations gravitaires post glaciaires en terrains métamorphiques. Comparaison des indices de déformation du versant sud de la Toura (Saint-Christophe-en-Oisans, France) avec le phénomène de rupture interne du versant sud du Mont Sec (Séchilienne, France), Bulletin of Engineering Geology and the Environment, 57(4), 387–395, https://doi.org/10.1007/s100640050062, 1999

Woods, T. L., Fullagar, P. D., Spruill, R. K., Sutton, L. C.: Strontium isotopes and major elements as tracers of ground water evolution: example from the Upper Castle Hayne Aquifer of North Carolina, Ground Water, 38(5), 762–771, https://doi.org/10.1111/j.1745-6584.2000.tb02712.x, 2000

Zeebe, R. E. and Wolf-Gladrow, D. A.: CO_2 in Seawater: Equilibrium, Kinetics, Isotopes, edited by Elsevier Oceanography Series, Amsterdam, 65, 2001.

930

935

940

945

950

955

960

965

970

975

Supplementary materials of

Landslides as geological hotspots of CO₂ emission: clues from the instrumented Séchilienne landslide, Western European Alps.

Pierre Nevers[1], Julien Bouchez[2], Jérome Gaillardet[2,4], Christophe Thomazo[3], Delphine Charpentier[1], Laëticia Faure[2] and Catherine Bertrand[1]

[1]UMR Chrono-Environnement 16 route de Gray, 25000 Besançon, France
[2]Université de Paris, Institut de physique du globe de Paris, CNRS, F-75005 Paris, France
[3]UMR CNRS/uB6282 Biogéosciences 6 Boulevard Gabriel, 21000 Dijon, France
[4]Institut Universitaire de France, 75231 Paris, France

Correspondence to: Pierre Nevers (*pierre.nevers@univ-fcomte.fr*)

1. **Petrological and mineralogical analysis of rock samples from the Séchilienne slope: thin sections and X-ray diffraction (XRD)**

1035

Sampling:

Samples used for this work were selected on the basis of their rock type, fracturation, and weathering degree in order to characterize the mineralogical, petrological, and geochemical modifications between fractured/weathered and unweathered samples of rocks from the same lithology. Thus, pairs and triplets of samples from the same lithology were collected, with various weathering degrees. The selected samples are represented as stars in the borehole logs (Fig. S1). Boreholes, as well as the lithological descriptions of the facies recovered by the core samples were carried out by the engineering consultant GEOTEC.

1040
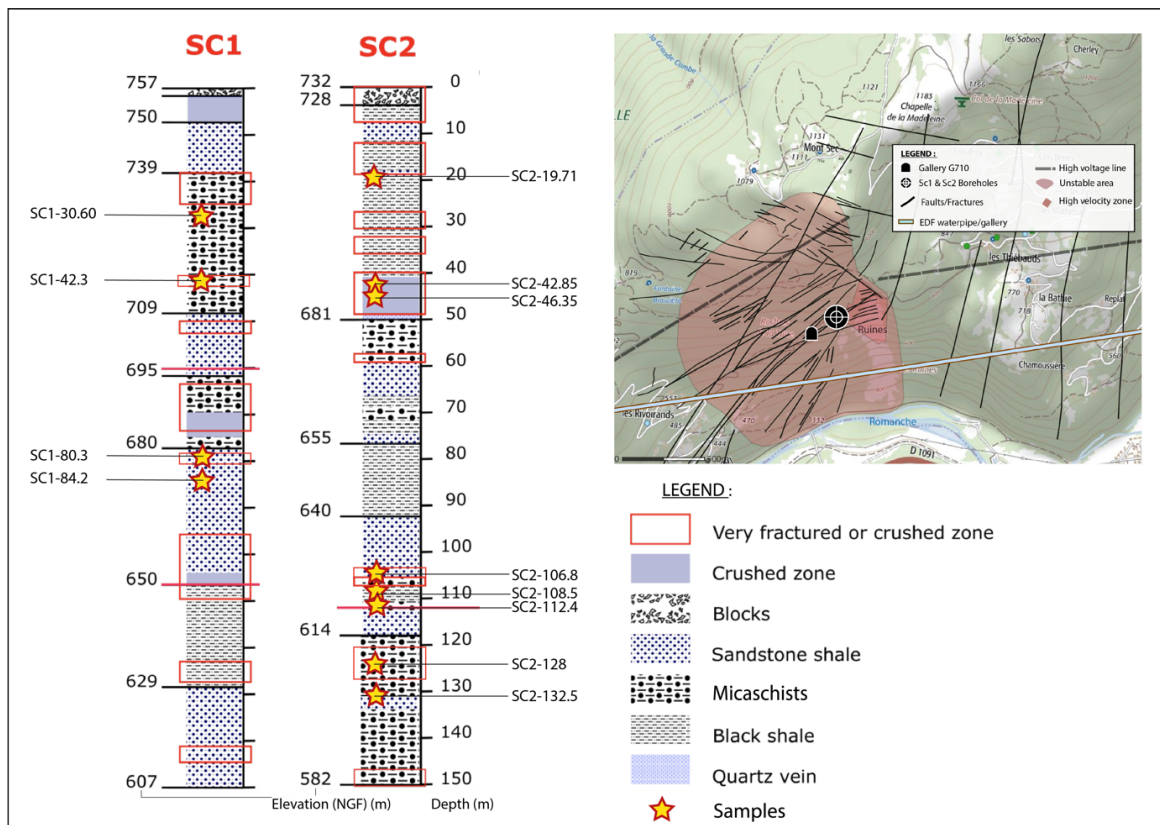
Figure S1: Boreholes SC1 and SC2 with location, lithology and analyzed samples location along the boreholes.

1045   On the SC1 borehole (Fig. S1), 2 pairs of samples we selected, *i.e.* 4 samples to be studied:

-   **(SC1 30.60 - 42.3)**: recovered from micaschists, are blue-grey colored and show brown weathering and oxidation shades, crossed by several quartz veins. These micaschists present decimetric fractured levels, notably between 40.15 and 45.00 m depth. SC1-30.60 is the unweathered sample and SC1-42.3 is the weathered sample.

1050   -   **(SC1 84.2 - 80.3)**: were sampled from massive, grey-blue micaschists with some pyrite and quartz, with punctual brown oxidation halos. From 79.20 to 81.40 m, a highly weathered and crushed zone is noticed within these micaschists. SC1-84.2 is the unweathered sample and SC1-80.3 is the weathered sample.

Two triplets and one pair of samples were selected from the second borehole (SC2), following the same logics as above. For the sample triplets, we selected one sample characterized as healthy and the other two were described as weathered:

1055   -   **(SC2 19.71 - 42.85 - 46.35)**: correspond to lustrous grey to black, vertically foliated and compact schists with quartz veins. The two altered samples are part of a very destructured and crushed zone with a brown to ochre clay matrix, made of weathered micaschist with sandstone occurrences, anthracite grey veins of quartz, hematite, goethite and disseminated pyrite. SC2-19.71 is the unweathered sample and SC2-42.85 and SC2-46.35 are the weathered samples.

1060

    -    **(SC2 108.5 - 106.8)**: correspond to a zone made of an alternance of schists and light grey sandstones, with occasional anthracite black schists. Numerous centimetric to decimetric quartz veins are present as well as highly fractured oxidized zones with ochre clayey fillings, mostly from 105.90 to 107.50 m, from which the weathered samples are taken. SC2-108.5 is the unweathered sample and SC2-106.8 is the weathered sample.

1065

    -    **(SC2 132.5 - 128 - 112.4)**: were sampled from light grey siliceous sandstones and shales, alternating with black shale levels. Numerous centimetric to decimetric quartz veins or interbeds and ochre oxidized fractures with red clayey fillings are noticed from 111.05 to 112.95 m. SC2-132.5 is the unweathered sample and SC2-128 and SC2-112.4 are the weathered samples.

1070   Thin sections from these samples are shown in Fig. S2-S4. Overall, the unweathered and weathered samples present the same mineralogy, i.e. quartz, white micas, alkali feldspar more or less weathered into a clay phase, and "opaques" corresponding to sulfides and oxides. Observations of these "opaques" in reflected light allow us to identify the presence of highly-oxidized pyrite and chalcopyrite. This oxidation is characterized by iron oxides such as hematite. The difference between unweathered samples and weathered samples is the fractional contribution of these minerals. Indeed, in weathered

1075   samples, larger amounts of white mica and with lesser amounts of alkali feldspar are found, as well as more hematite. Weathered samples present oxidized pyrite and chalcopyrite, which are not oxidized in the unweathered samples. Regarding the structures the sample, we do not observe any real difference between weathered and unweathered samples, except for the pair SC1 132.5 - 128 which seems to present a foliation for the fractured and weathered samples. This foliation is underlined by the white mica, forming flaps (figures S2 - S4).

1080
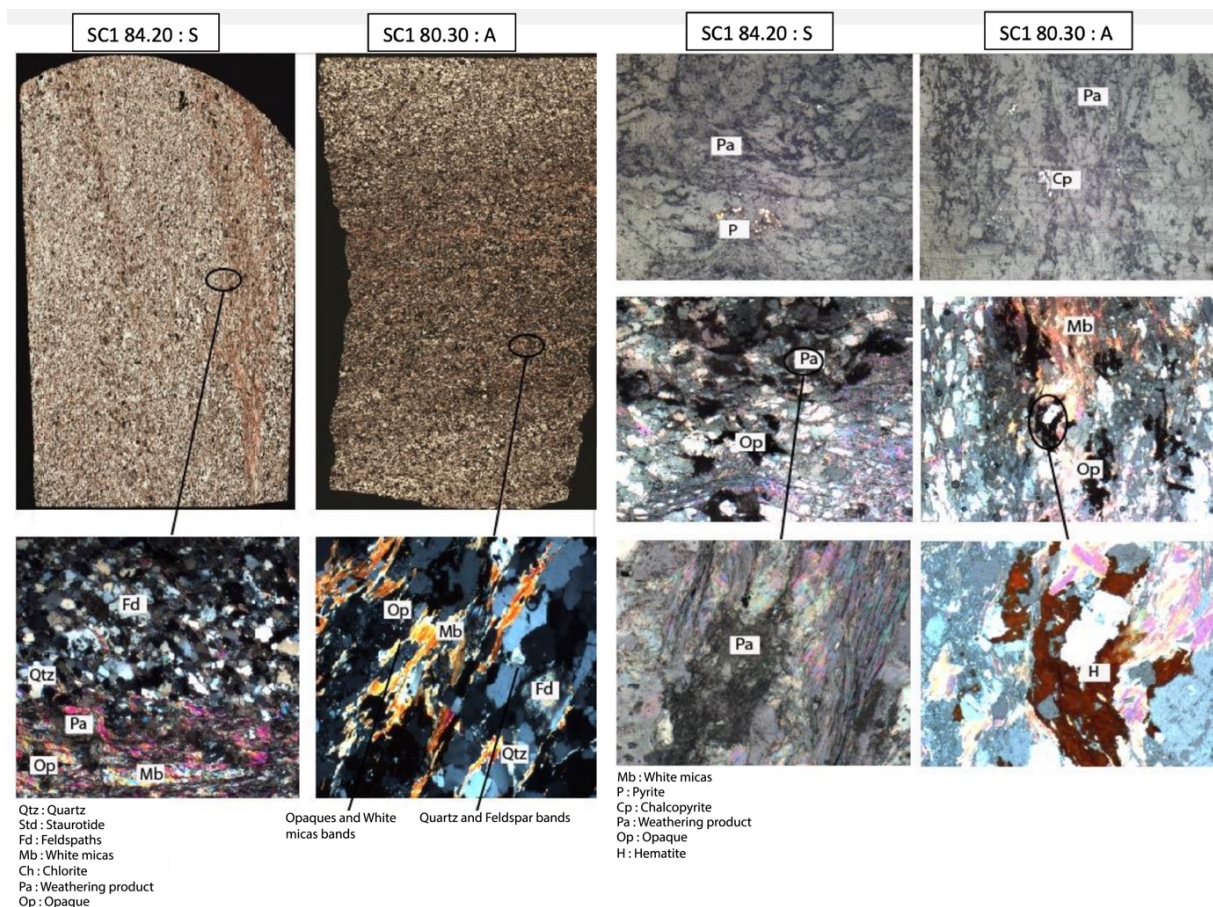
Figure S2: Thin sections photographs and mineralogy SC1 84.20-80.30
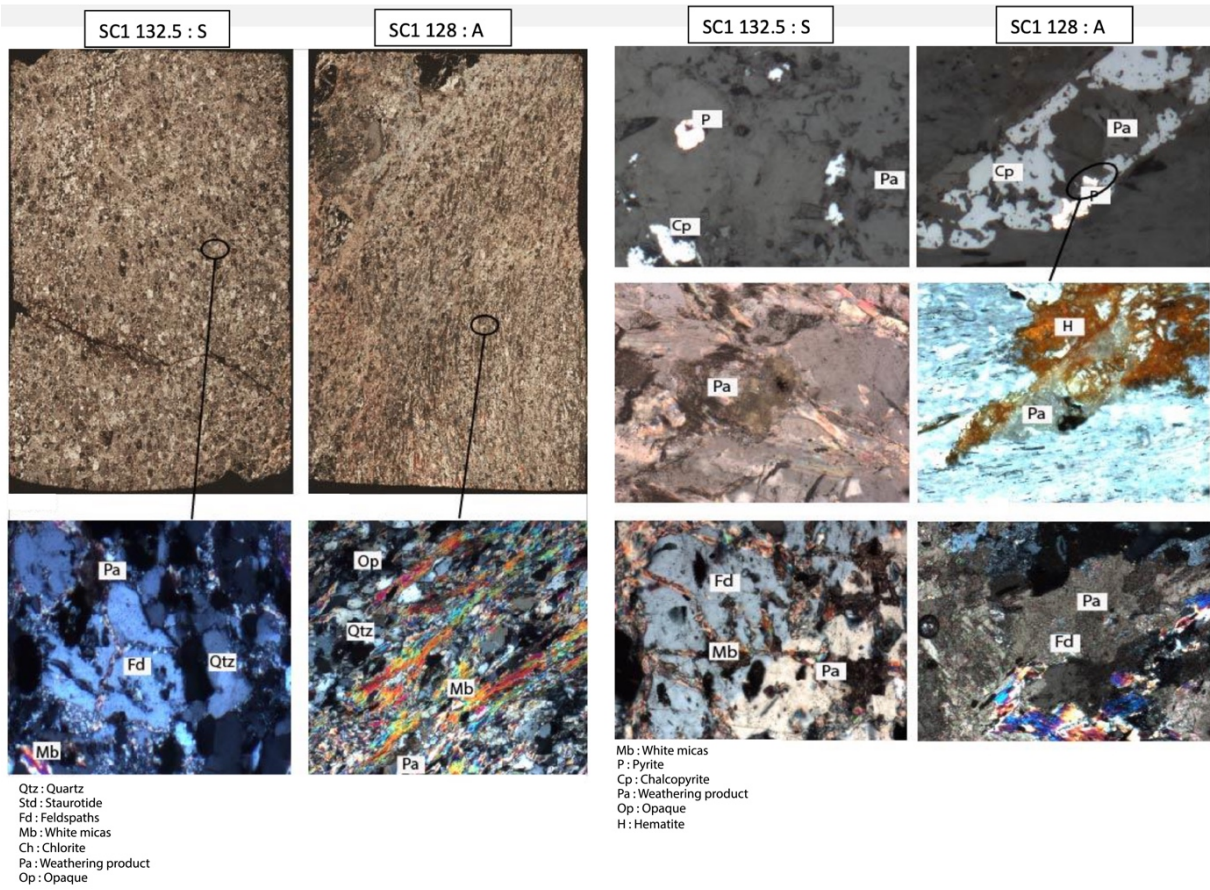
Figure S3: Thin sections photographs and mineralogy SC1 132.5-128
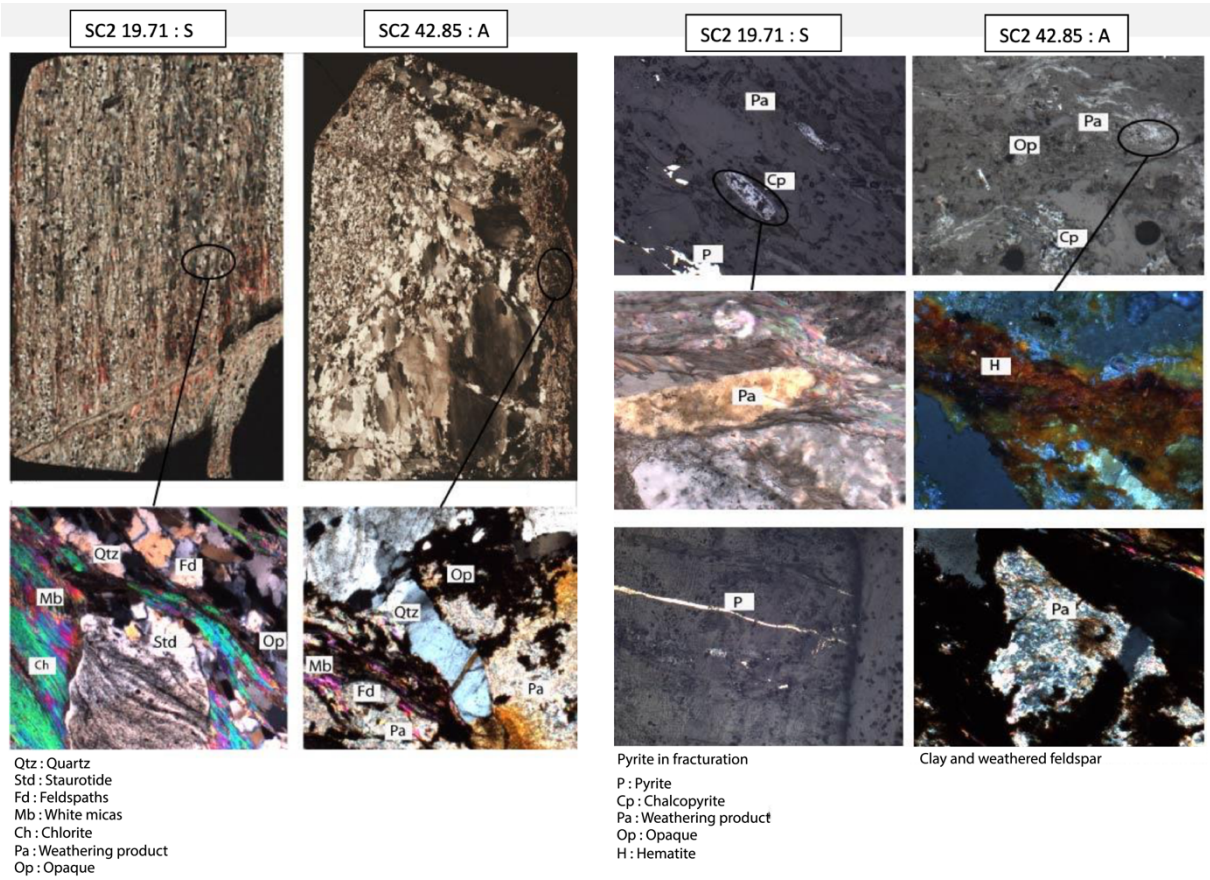
Figure S4: Thin sections photographs and mineralogy SC2 19.71-42.85

XRD analyses show that illite is the main type of white mica present in these samples, while albite and orthose are present as alkali feldspar (figures S5 - S7). Because of their low abundance in the samples, sulfides and oxides visible in thin sections are not to prominent in XRD. Overall, we observe lower amounts (up to complete disappearance) of orthose in the weathered samples compared to unweathered samples. In weathered samples, an increase of the proportion of illite and the appearance of hematite is evidenced (figures S5 - S7).

1090

1095

1100
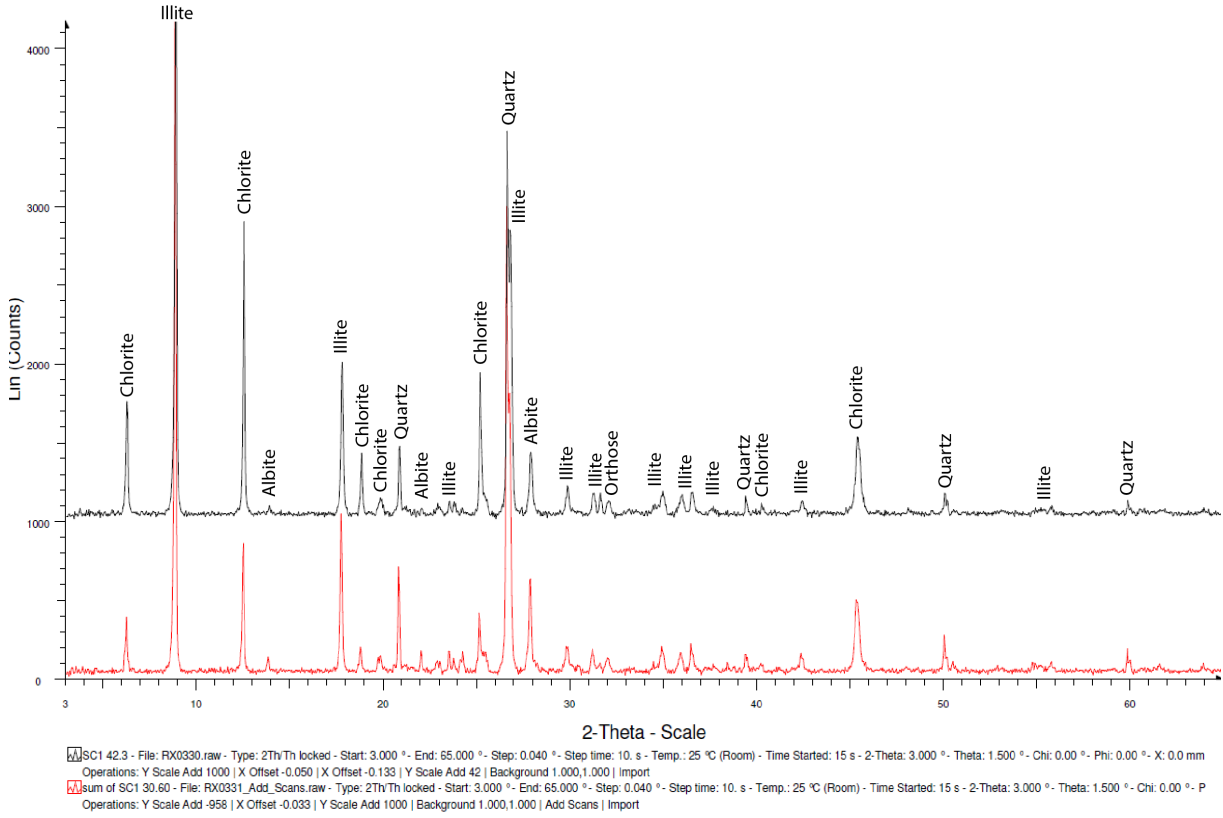
Figure S5: X-ray diffraction spectra SC1 30.60-42.30 / SC1 84.20-80.30
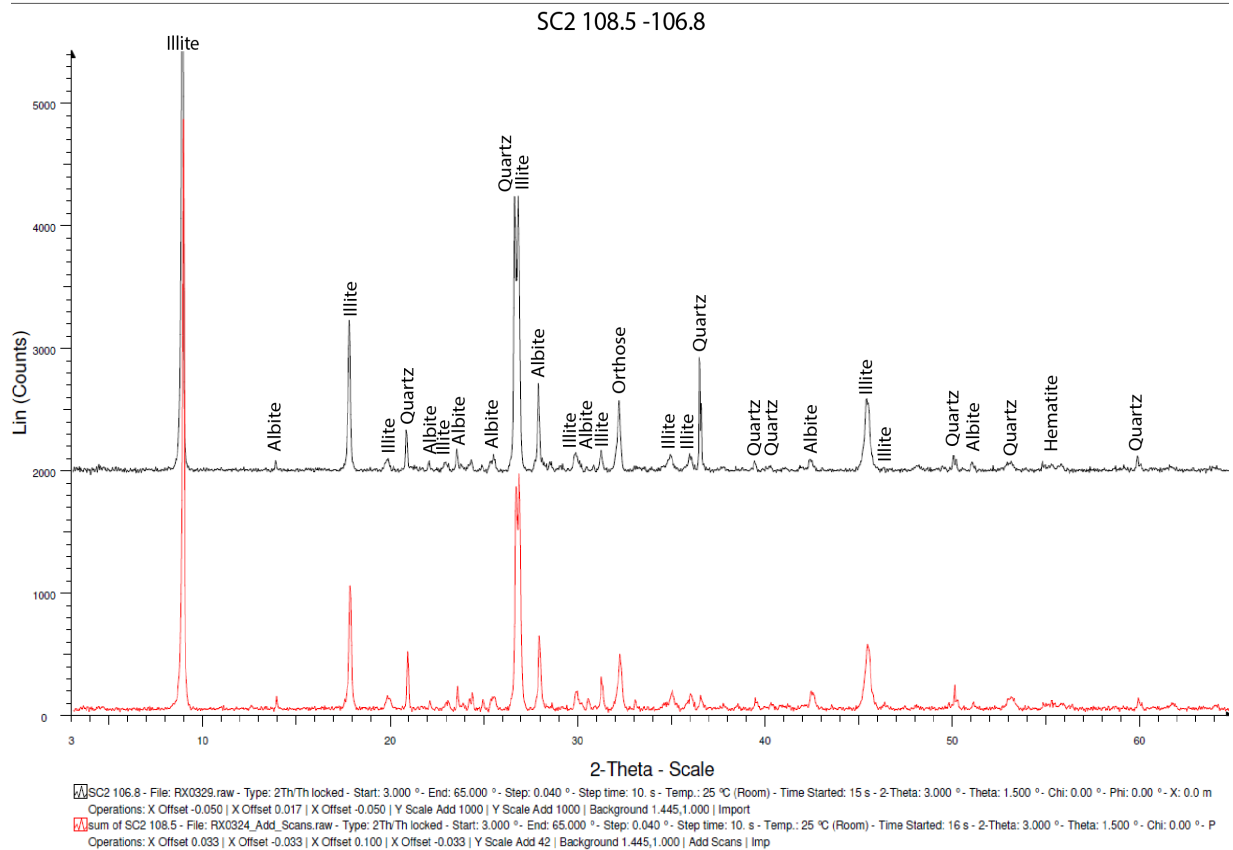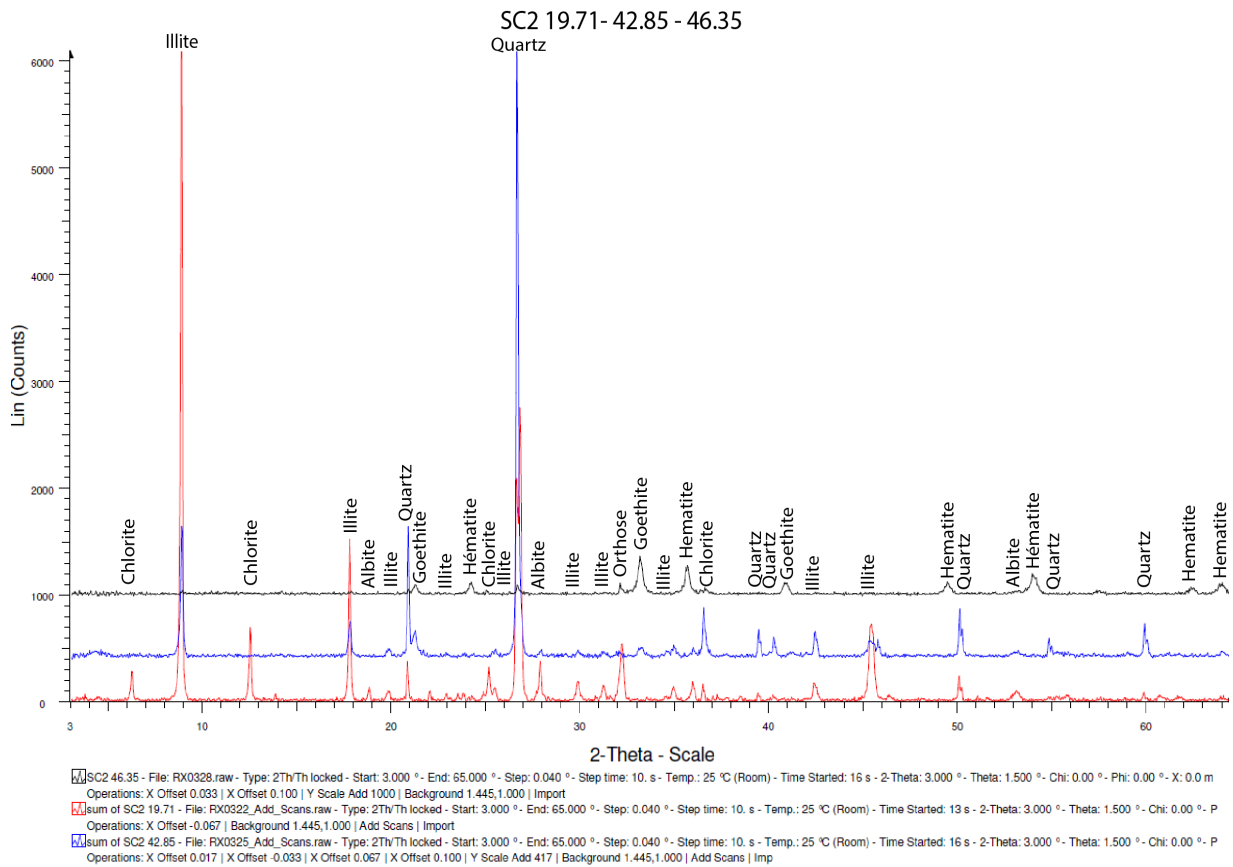
Figure S6: X-ray diffraction spectra SC2 19.71-42.85-46.35 / SC2 108.5-106.8

105
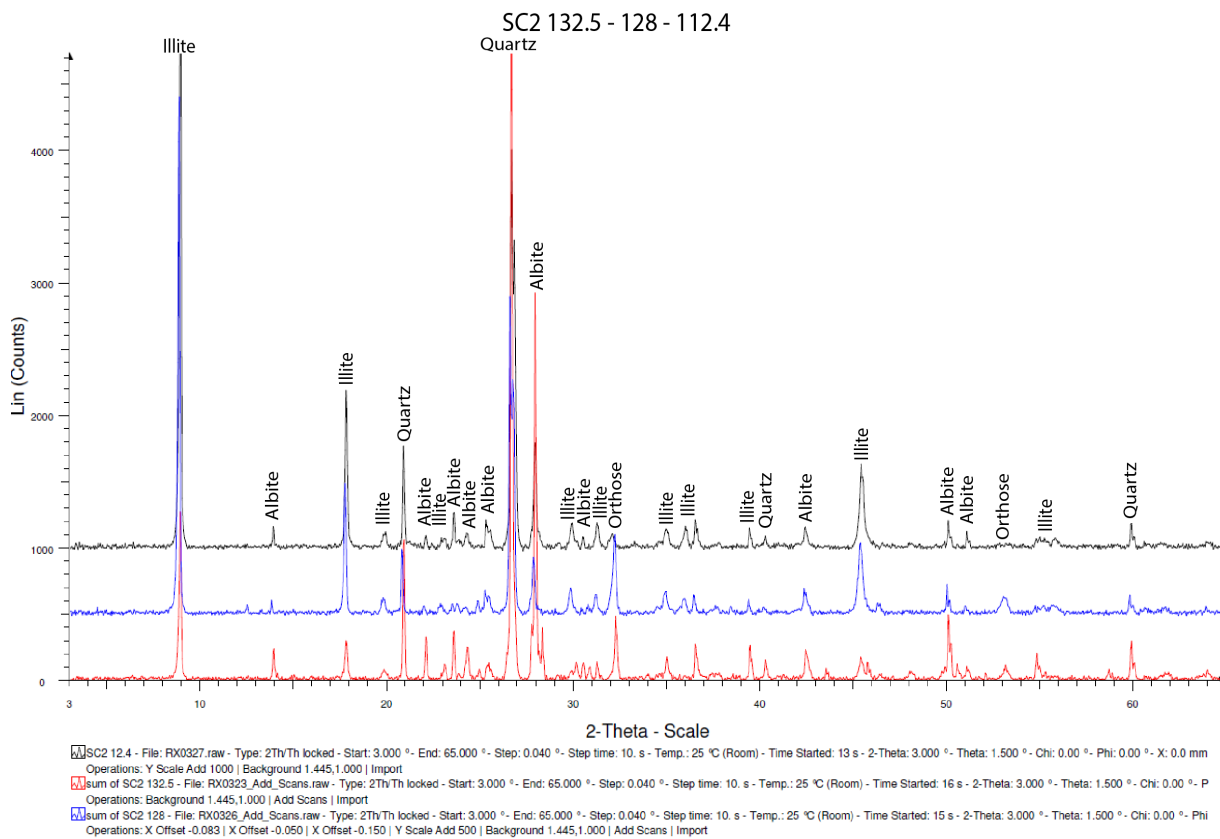
Figure S7: X-ray diffraction spectra SC2 132.5-128-112.4

110

115

120

125

2. Identifying chloride inputs (atmospheric, anthropogenic, salts): X *vs.* Cl diagrams
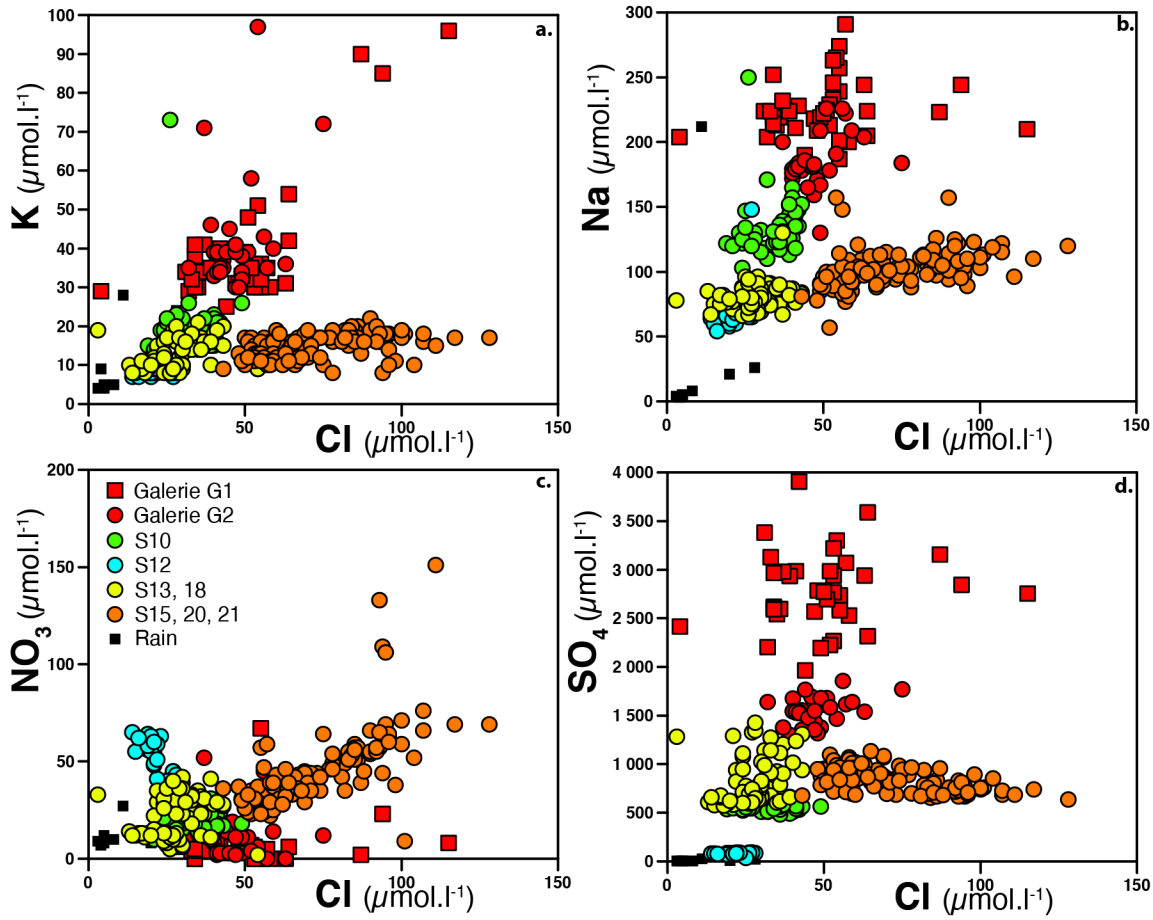
Figure S8: Elemental concentrations (X) of the different groups of water outflow from the Séchilienne massif as a function of Cl concentrations; a. K *vs.* Cl, b. Na *vs.* Cl, c. NO_3 *vs.* Cl, d. SO_4 *vs.* Cl. These diagrams are used in the section 5.1.1. of the main text.

3.   Solving the mixing equations

Model set-up and Sr fractions

Given the discussion of section 5.1 and the geochemical mixing diagrams presented in Fig. 4, three end members can be identified to release solutes to the springs of the Séchilienne area: silicate weathering (*sil*), carbonate weathering (*carb*; including both calcite and dolomite), and gypsum dissolution (*gyps*). The contribution of each of these processes to the solute load of the springs can be estimated using a combination of mixing equations, provided that geochemical tracers that are conservative during mixing of compositionally different waters can be identified, and that the composition of the end members can be assessed. He we use two such tracers: $^{87}Sr/^{86}Sr$ and Na/Sr ratios (all corrected from rain and anthropogenic inputs, as explained in the main text). Indeed, the $^{87}Sr/^{86}Sr$ ratio is not affected by isotope fractionation due to the way data are reduced after measurements by mass spectrometry; and both Na and Sr are soluble elements unlikely to be scavenged into secondary solids such as clays in most contexts. Two mixing equations, each based on one of the two tracers, can be combined with a third summation equation to solve for X_{sil}^{Sr}, X_{carb}^{Sr}, and X_{gyps}^{Sr}, the relative contribution of the three identified end member to dissolved Sr:

$$\left(\frac{^{87}Sr}{^{86}Sr}\right)_{spring} = X_{sil}^{Sr}\left(\frac{^{87}Sr}{^{86}Sr}\right)_{sil} + X_{carb}^{Sr}\left(\frac{^{87}Sr}{^{86}Sr}\right)_{carb} + X_{gyps}^{Sr}\left(\frac{^{87}Sr}{^{86}Sr}\right)_{gyps} \tag{S1}$$

$$\left(\frac{Na}{Sr}\right)_{spring} = X_{sil}^{Sr}\left(\frac{Na}{Sr}\right)_{sil} + X_{carb}^{Sr}\left(\frac{Na}{Sr}\right)_{carb} + X_{gyps}^{Sr}\left(\frac{Na}{Sr}\right)_{gyps} = X_{sil}^{Sr}\left(\frac{Na}{Sr}\right)_{sil} \tag{S2}$$

$$X_{sil}^{Sr} + X_{carb}^{Sr} + X_{gyps}^{Sr} = 1 \tag{S3}$$

The simplification of eq. (S2) is made possible by the fact that the gypsum and carbonate end members can be assumed to be devoid of Na. This assumption is supported by the positions of the different springs in a Na/Sr *vs.* $^{87}Sr/^{86}Sr$, which indicates that the low-$^{87}Sr/^{86}Sr$ component, encompassing both carbonate and gypsum weathering of the springs has a negligible Na content, with the exception of spring S12 which we do not treat quantitatively here (Fig. S9).
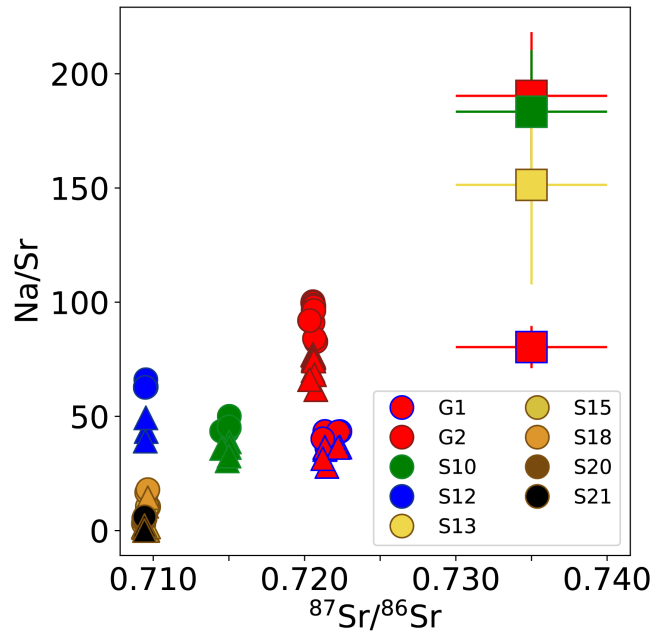
Figure S9: Na/Sr vs $^{87}Sr/^{86}Sr$ for the different groups of water outflows (circles represent spring water composition corrected for rain and anthropogenic inputs (eq. 1); triangles represent spring water composition corrected for gypsum dissolution sampled in the Séchilienne massif. The inferred composition of the silicate end member for each group is shown as squares

The composition of the end members was constrained as follows (values also provided in Table S1):

- for each spring, $\left(\frac{^{87}Sr}{^{86}Sr}\right)_{spring}$ and $\left(\frac{Na}{Sr}\right)_{spring}$ were taken to be equal to the average ratios (corrected from rain inputs for Na/Sr) over all measurements available for the spring (note that one outlier were dismissed for each of the two springs G1 and G2);

- $\left(\frac{^{87}Sr}{^{86}Sr}\right)_{carb}$ was taken between 0.7090 and 0.7095 or 0.7095 and 0.7105, depending on whether the carbonate end member was assumed to be of calcitic or dolomitic nature. These ranges were constrained based on our own geochemical analyses of rock samples (Tab. 1; data available at 10.5281/zenodo.4606732). Note that the first range is consistent with what is known of early Jurassic seawater Sr isotope composition (MacArthur and Howarth, 2004). $\left(\frac{^{87}Sr}{^{86}Sr}\right)_{gyp}$ was taken between 0.7075 and 0.7080, which is typical of Triassic seawater, and in agreement with values reported for Alpine gyspum by previous studies (Kloppmann et al., 2017).

- $\left(\frac{^{87}Sr}{^{86}Sr}\right)_{sil}$ was assumed to be equal to the highest measured Sr isotope ratio throughout the local bedrock samples ("micaschist", 0.735 ± 0.005; Tab. 1).

- To determine the $\left(\frac{Na}{Sr}\right)_{sil}$ ratio for each of the springs the most affected by silicate weathering (G1, G2, and S10), we extrapolated the Na/Sr *vs.* $^{87}Sr/^{86}Sr$ relationships passing through (1) the carbonate end member ($^{87}Sr/^{86}Sr$ = 0.7090-0.7105 and Na/Sr = 0) and (2) the samples collected for this spring (Fig. S9) to a $^{87}Sr/^{86}Sr$ equal to that of the silicate end member (0.735, see above). Linear extrapolation in this diagram is made possible by the fact that Sr concentration is present on the denominator of both ratios plotted. Note that following the discussion on Cl sources in section 5.1.1 of the main text, for each of the springs G1, G2, and S10 two estimations of $\left(\frac{Na}{Sr}\right)_{sil}$ were performed: one based on Na concentrations corrected from rain inputs only following eq. (1) (*[Na*]*), and the other assuming that the entirety of Cl⁻ release to the springs was associated with Na⁺ release (*[Na]-[Cl]*). The average between these two estimates was then used for further calculations. The obtained $\left(\frac{Na}{Sr}\right)_{sil}$ values range from 80 ± 9 to 205 ± 30 mol/mol, lower than those classically estimated for silicates (e.g. Négrel et al., 1993) but consistently with the fact that the parent rock at Séchilienne is a micaschist, that is a sedimentary rock that has lost soluble elements such as Na in previous weathering episodes compared to igneous silicates. For the springs the least affected by silicate weathering (S12, S13, S15, S18, S20, and S21), as such extrapolation would lack precision, we simply took the average and standard deviation of the $\left(\frac{Na}{Sr}\right)_{sil}$ ratios estimated for springs G1, G2, and S10 (yielding 162 ± 40). This strong assumption does not bear consequence on our overall evaluation as these former springs are not significantly affected by silicate weathering anyway.

The uncertainty on the different input parameters was propagated to the output variables (X_{sil}^{Sr}, X_{carb}^{Sr}, and X_{gyp}^{Sr}) using a Monte Carlo method based on 10,000 iterations. For this, at each of the 10,000 iterations a value for each input parameter (end member composition) was randomly picked following either (a) a normal distribution with mean equal and standard deviations to the estimate and uncertainty provided above, respectively, for parameters $\left(\frac{^{87}Sr}{^{86}Sr}\right)_{sil}$ and $\left(\frac{Na}{Sr}\right)_{sil}$; and (b) a uniform distribution bounded by the lowest and highest estimates provided above for parameters $\left(\frac{^{87}Sr}{^{86}Sr}\right)_{carb}$ and $\left(\frac{^{87}Sr}{^{86}Sr}\right)_{gyp}$.

The choice of a uniform distribution to reflect uncertainty on the latter parameters is justified by the fact that it is highly unlikely that Sr isotope ratios of marine carbonates lie outside of the prescribed range, which is unavoidable to occur for a significant number of random draws if one were to be used a normal distribution with a reasonable standard deviation instead. Note that, generally speaking, the composition of the springs was not considered as a random variable here and was simply fixed for all iterations. However, in order to account for uncertainty on the Cl⁻ source to the spring waters (main text section 5.1.1), for each spring and for each simulation we randomly drew values of $\left(\frac{Na}{Sr}\right)_{spring}$ following a uniform distribution bounded by $[Na*]$ and $[Na]-[Cl]$. Finally, Monte Carlo runs yielding X_{sil}^{Sr}, X_{carb}^{Sr}, and X_{gyp}^{Sr} values outside of the range $[0,1]$ were dismissed (the number of "valid" iterations is reported in Table S2).

The resulting distributions of output X_{sil}^{i} values are reported in Table S2 as their 16th, 50th (median), and 84th percentile. Median estimates of X_{sil}^{Sr} range from 0.06 and 0,08 (springs S15 and S18) to 0.42 and 0.47 (springs G2 and G1, respectively); median estimates of X_{carb}^{Sr} range from 0.04 and 0.07 (springs S15 and S18) to 0.36 (spring S10); and median estimates of X_{gyp}^{Sr} range from 0.25 and 0.29 for G1 and G2 to 0,85-0,90 for S18-S15. S10 median estimate is 0.42. Obtained values differed weakly depending on whether a calcitic or a dolomitic composition was used for $\left(\frac{^{87}Sr}{^{86}Sr}\right)_{carb}$ (Tab. S2).

Gypsum contribution

The contribution of each of these end members to the load of the dissolved major species SO₄, Ca, and Mg is necessary to evaluate the impact of the different weathering processes to the CO₂ budget of the Séchilienne area (Torres et al., 2016). In principle, these end member contributions to major dissolved species can be calculated from the corresponding contributions to dissolved Sr following:

$$X_i^E = X_i^{Sr} \left(\frac{E}{Sr}\right)_i / \left(\frac{E}{Sr}\right)_{spring} \tag{S4}$$

with $i = sil, carb,$ or gyp, and $E = $ SO₄ and Mg (corrected for rain and anthropogenic inputs). As explained below, because secondary carbonate formation might occur at Séchilienne and thus lead to the preferential scavenging of Ca from waters, eq. (S4) cannot be used indifferently for $E = $ Ca or for $i = carb$. We return to the estimation of X_i^{Ca} values later. Regardless of this issue, eq. (S4) can first be used to calculate X_{gyp}^{Mg} and X_{gyp}^{SO4} provided that the $\left(\frac{E}{Sr}\right)_{gyp}$ ratios are known. The E/Sr ratios of the gypsum end member were determined using the E/SO₄ *vs.* (Ca+Mg)/SO₄ relationships described by the springs the least affected by silicate weathering (as identified by their low ⁸⁷Sr/⁸⁶Sr ratios, *i.e.* springs S13, S15, S18, S20, and S21; Fig. S10). Indeed, for these springs where sulfate can be assumed to be entirely derived from gypsum and not from sulfide dissolution, at (Ca+Mg)/SO₄ of 1 mol/mol, the entirety of the dissolved load can be assumed to be derived from gypsum dissolution alone (Ca and Mg being the two major cations likely to be released by gypsum dissolution).
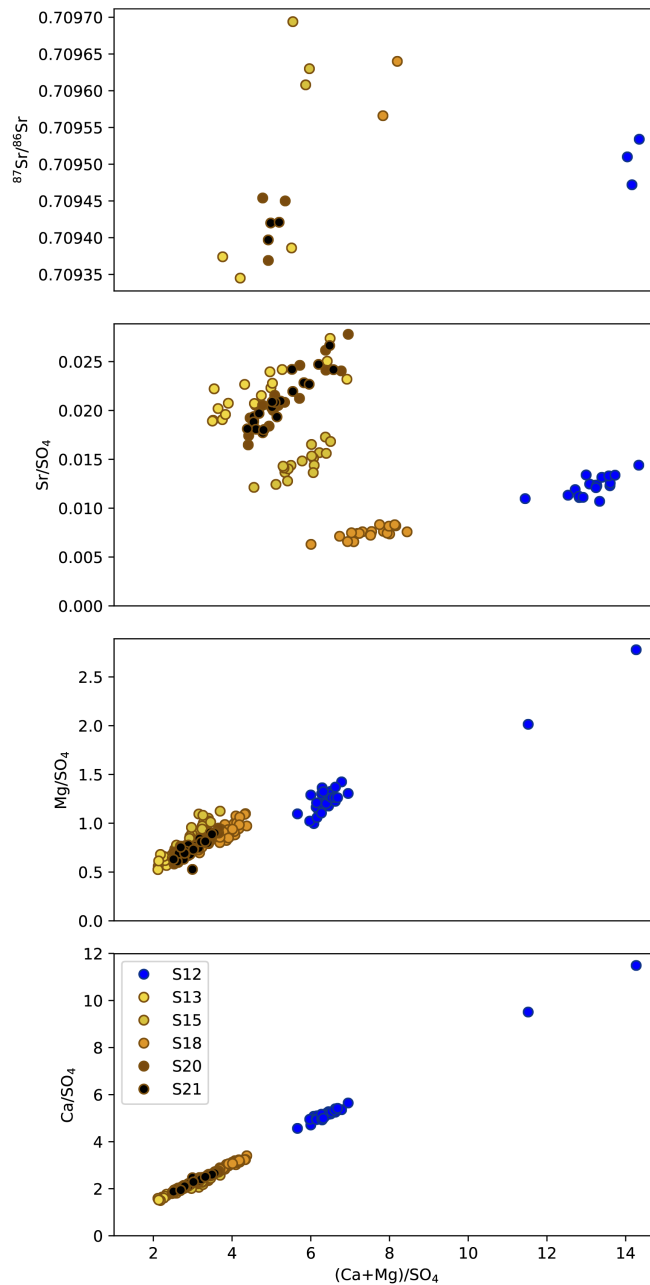
Figure S10: Mixing diagrams of the $^{87}Sr/^{86}Sr$ ratio and the E/SO_4 (with E = Sr, Mg, Ca, and Na) molar ratio *vs*. the $(Ca+Mg)/SO_4$ molar ratios, used to determine the E/Sr molar ratios of the gypsum end member.

1250

Linear extrapolation in Fig. S10 is made possible by the fact that SO_4 concentration is present on the denominator of both ratios plotted. Taking the average values obtained through extrapolation of the observed trends to $(Ca+Mg)/SO_4 = 1$ mol/mol suggests 0.31 ± 0.04 and $9.2 \ 10^{-3} \pm 4.4 \ 10^{-3}$ mol/mol for the Mg/SO_4 and Sr/SO_4 ratios of the gyspum end members. From these two SO_4-normalized ratios, Sr-normalized ratios can be obtained to calculate X_{gyp}^{Mg} and X_{gyp}^{SO4} using eq. (S4). Obtained

1255 modal values of X_{gyp}^{Mg} are lower than 0.03 for springs G1-G2-S10, and around 0.20-0.40 for the other springs. Modal values of X_{gyp}^{SO4} are lower than 0.05 for springs G1-G2-S10, and range between 0.5 and 0.75 for the other springs.

As the SO_4/Sr ratio of the carbonate end member was assumed to be equal to 0, consistently with the mixing diagrams of Fig. 4, X_{sil}^{SO4} could be calculated as $1 - X_{gyp}^{SO4}$ (eq. S3). Consequently, a value for the SO4/Sr ratio of the silicate end member could be estimated using the SO4/Sr mixing equation (similar to eqs. (S1-S2)):

1260

$$\left(\frac{SO_4}{Sr}\right)_{spring} = X_{sil}^{Sr}\left(\frac{SO_4}{Sr}\right)_{sil} + X_{gyp}^{Sr}\left(\frac{SO_4}{Sr}\right)_{gyp} \tag{S5}$$

To solve eq. (S5), the average and standard deviation of all measurements of $\left(\frac{SO_4}{Sr}\right)_{spring}$ were used, thereby yielding a spring-specific value for $\left(\frac{SO_4}{Sr}\right)_{sil}$. This estimate was performed during the Monte Carlo iterations described above, yielding modal values ranging from 666 (spring S20) to 1,845 mol/mol (spring G2).

Secondary carbonate formation and carbonate contribution

The precipitation of secondary carbonates is known to preferentially scavenge dissolved Ca^{2+} at the expense of other alkali-earth ions Mg^{2+} and Sr^{2+} (Bickle et al., 2015). As a consequence, Ca does not necessarily behave conservatively in carbonate-rich settings such as Séchilienne, where secondary carbonate precipitation is likely to occur. We quantify the role of secondary carbonate formation using the method proposed by Bickle et al. (2015), which is based on the comparison between the chemical composition of springs and that predicted from conservative mixing between the rock dissolution end members. The Rayleigh-type equation proposed by Bickle et al. (2015) links dissolved E/Ca ratios to the extent of Ca scavenging by the formation of secondary carbonates:

$$\left(\frac{E}{Ca}\right)_p = \left(\frac{E}{Ca}\right)_0 \gamma^{K_d^E - 1} \tag{S6}$$

where $\left(\frac{E}{Ca}\right)_0$ is the "initial" E/Ca ratios of waters (*i.e.*, before secondary carbonate precipitation has taken place) with E = Sr, Mg, or Na, $\left(\frac{E}{Ca}\right)_p$ is the E/Ca ratios of waters after secondary carbonate precipitation has taken place, γ is the amount of "initial" Ca left in solution after secondary carbonate precipitation has taken place, and K_d^E is the partition coefficient of element E into calcite, defined as the ratio between the E/Ca ratio into the precipitating calcite and that in water. During our Monte Carlo simulations, we randomly drew values for K_d^{Sr} and K_d^{Mg} following a uniform distribution between 0.02 and 0.10, and considered that $K_d^{Na} = 0$. As explained by Bickle et al. (2015), results in terms of source apportionment do not depend strongly on the exact values chosen for the K_d^E parameters.

In a first set of attempts we assumed that secondary carbonate precipitation at Séchilienne was affecting only waters and solutes derived from two of the three rock dissolution end members (*i.e.* silicate and carbonate rocks, silicate rocks and gypsum, or carbonate rocks and gypsum). We assume that secondary carbonate precipitation affects solutes derived from the three weathering sources (carbonate, silicate, and gypsum dissolution) after they are mixed. Such scenario probably does not reflect perfectly the reality of the interplay between water mixing and chemical reactions in the subsurface at Séchilienne, but account for the fact that solutes from the three rock dissolution end members are mixed in a complex porous media, while keeping this problem mathematically tractable.

In the compositional Sr/Ca-Mg/Ca-Na/Ca space, the mixing array between carbonate, silicate, and gypsum dissolution is a plane, to which the composition of the springs can be "brought back" (Bickle et al., 2015):

$$\alpha \gamma^{1-K_d^{Mg}}\left(\frac{Mg}{Ca}\right)_p + \beta \gamma^{1-K_d^{Sr}}\left(\frac{Sr}{Ca}\right)_p + \varepsilon \gamma \left(\frac{Na}{Ca}\right)_p = \delta \tag{S7}$$

where α, β, ε, and δ are the parameters of the Cartesian equation of the mixing plane in the Sr/Ca-Mg/Ca-Na/Ca space. Note that eq. (S7) is valid because Na is not significantly incorporated into secondary carbonates (in other words, K_d^{Na} is assumed to be equal to 0). The ternary mixing relationships in the Sr/Ca-Mg/Na-Na/Ca space were constrained for Séchilienne using our own geochemical analyses of rock samples (Tab. 1) and are shown in Fig. S11. These relationships thus allow us to solve numerically eq. (S7) for γ for each spring. We performed this calculation for various values of the relative contribution of dolomite dissolution to the overall Ca released to solution by carbonate weathering (from 0% to 100% dolomite, the rest being delivered by calcite dissolution; the two extreme cases are illustrated in Fig. S11), and constrained the chemical ratios of each of the carbonate components by our own geochemical analyses of rock samples (Tab. 1). We observed as a general trend that increasing the relative contribution of the dolomite end member beyond 20% resulted in an extent of alkalinity consumption through carbonate precipitation that was too large compared to alkalinity production to be sustainable. As a consequence, we fixed the relative contribution of dolomite to the overall Ca release by carbonate dissolution to 10% in the following calculations.

With these constraints, across the Monte Carlo simulations median estimates of γ are 0.38 for G1, 0.39 for G2, 0.40 for S10, and 0.90 for S15. For the other springs, γ was set to 1.00 as no Ca scavenging was required to explain the data - in other words, for these springs the hydrochemical data approximately lie on the mixing plane between the three rock dissolution end members in the Sr/Ca-Mg/Ca-Na/Ca compositional space.

The γ value found for each spring can then be used to provide a value for the dissolved Sr/Ca, Mg/Ca, and Na/Ca ratios before the carbonate precipitation has taken place $\left(\frac{E}{Ca}\right)_0$ using eq. (S6) with the measured spring ratios as values for $\left(\frac{E}{Ca}\right)_p$. Then, X_{carb}^{Ca} and X_{carb}^{Mg} can be estimated from eq. (S4) for $i = carb$, but using the above-inferred Ca/Sr and Mg/Sr ratios (calculated from Sr/Ca and Mg/Ca ratios) before secondary carbonate precipitation as values of $\left(\frac{E}{Sr}\right)_{spring}$. X_{sil}^{Ca} and X_{sil}^{Mg} are then determined by difference using eq. (S3) with Ca or Mg instead of Na, Finally, knowing the composition of the carbonate end member (as constrained by our geochemical analyses on rock samples; Tab. 1), values for $\left(\frac{Ca}{Sr}\right)_{sil}$ and $\left(\frac{Mg}{Sr}\right)_{sil}$ can be determined using eq. (S2) with Ca and Mg instead of Na, respectively.
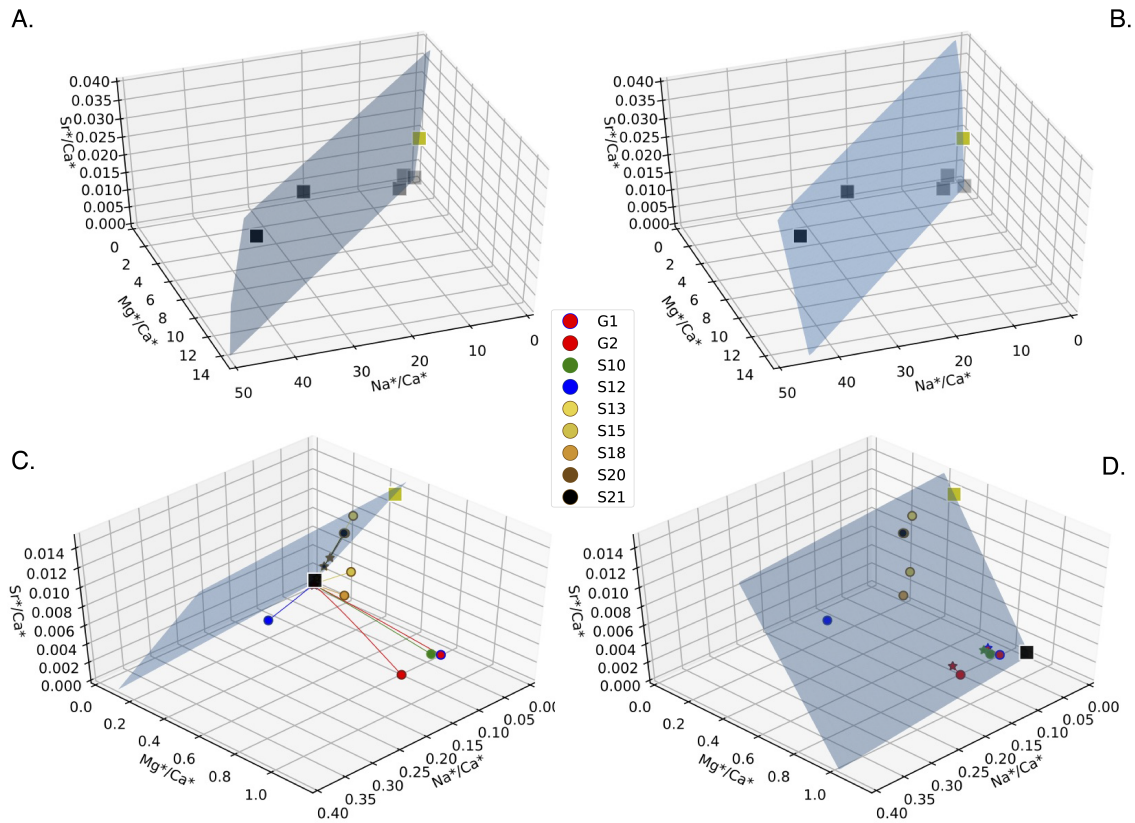
Figure S11: Quantification of the extent of secondary carbonate precipitation on dissolved Ca scavenging,. Circles represent spring water composition corrected for rain and anthropogenic inputs (eq. 1) and stars represent spring water composition corrected for secondary carbonate precipitation (hence resulting from conservative mixing only) using the method of Bickle et al. (2015) (eq. S7). The blue plane reflects the ternary mixing between waters derived from carbonate, silicate and evaporite dissolution, as constrained by our geochemical analyses of rocks samples (Tab. 1), on which spring composition must lie after correction from the effect of secondary carbonate precipitation. To obtain these results, all spring Cl^- was assumed to be associated to Na^+ (main text section 5.1.1), and K_d^{Sr} was assumed to be equal to K_d^{Mg} with a value of 0.06 was used.

To assess the validity of our findings from the mixing model using independent measurements, our $\delta^{34}S$ measurements can be used. A significant linear negative relationship ($R^2 = 0.8$) exists between the $\delta^{34}S$ measured in springs across the Séchilienne massif and the modal estimates of their X_{sil}^{SO4}, consistent with the isotope composition of sulfur being driven by a binary mixture (Tab. S3; Fig. S12). The intercept of this relationship ($X_{sil}^{SO4} = 0$, equivalent to $X_{gyp}^{SO4} = 1$) yields an estimate for $\delta^{34}S_{gyp} = 8.4‰$, while extrapolation to $X_{sil}^{SO4} = 1$ indicates $\delta^{34}S_{sulfur} = -3.1‰$. Such estimates are fully consistent with our own measurements of solid sulfur at Séchilienne, as well as with reported measurements for Triassic seawater where local gypsum might have formed.
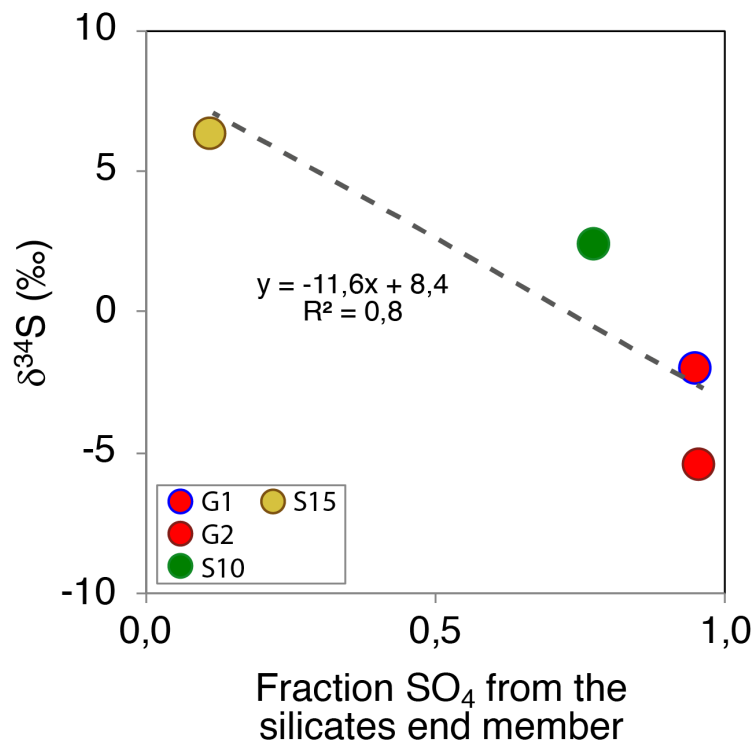
Figure S12: δ³⁴S measured in springs across the Séchilienne massif vs modal estimates of their fraction of SO₄ from silicate endmember: X_{sil}^{SO4}.

CO₂ consumption budget

The mixing analysis presented above shows that at Séchilienne solutes are released to springs through the partial dissolution of silicate minerals, carbonate minerals, and gypsum, while dissolved Ca is scavenged by secondary carbonate precipitation. Fundamentally, these weathering reactions modify the carbon content in the atmosphere-hydrosphere continuum, which impacts the CO₂ concentration in the atmosphere. An approach to evaluate this impact has been recently proposed by Torres et al. (2016), based on the relative change in alkalinity (Alk) and Dissolved Inorganic Carbon (DIC) in ambient waters resulting from the combination of weathering reactions. Torres et al. (2016) contend that the relevant Alk/DIC ratio against which the shifts in Alk and DIC ensuing weathering reactions have to be evaluated is that of the ocean.

However, the approach proposed by Torres et al. (2016) cannot be used in the case of Séchilienne, in particular because secondary carbonate precipitation is a significant process there. Indeed, secondary carbonate precipitation removes Alk and DIC from ambient waters following the reaction:

$$Ca^{2+} + 2HCO_3^- \rightarrow CaCO_3 + H_2CO_3 \hspace{3cm} (S9)$$

And the ensuing change in Alk and DIC occurs at the loci of secondary carbonate precipitation (i.e. at Séchilienne, in the subsurface of the instability), the Alk/DIC of which is not known. However, we still believe that it is essential to assess the long-term (that is, once weathering-derived solutes are delivered to the oceans) effects of these weathering reactions on atmospheric CO₂, especially in contexts where sulfide oxidation is a significant process, such as at Séchilienne.

As a consequence, we assess the CO₂ impact of the various weathering reactions at Séchilienne in the following way (Tab. S3):

- For silicate weathering by carbonic acid (eq. 9 of main text), each meq of cation released leads to the consumption of 1 mole of CO_2 "on site", meaning immediately when the reaction takes place; and we assume that all meq of cation released are precipitated in the ocean on the "long term" through equation (S9), leading in total to the net consumption of 0.5 mole of CO_2 per meq initially released;

- Silicate weathering by sulfuric acid (eq. 10), has no "on site" net effect on atmospheric CO_2; and we assume that it has no net effect on the "long term" either once solutes are delivered to the ocean, based on the fact that this reaction does not produce any alkalinity that is required for carbonate precipitation to occur (eq. S9);

- Carbonate weathering by carbonic acid (eq. 11 of main text) consumes 0.5 mol of CO_2 per meq of cation (Ca^{2+} or Mg^{2+}) released "on site", but this effect is negated on the "long term" by carbonate precipitation in the ocean (eq. S9; note that here "long term" refers to a time scale longer than the characteristic time scale for carbonate precipitation in the ocean (around 10^5 yrs), but shorter that the characteristic time scale for sulfate reduction in the ocean (around 10^7 yrs; Torres et al., 2016));

- Carbonate weathering by sulfuric acid (eq. 12 of main text) has no "on site" net effect on atmospheric CO_2; but is likely to lead on the long term to the release of 0.25 mol of CO_2 (eq. S9) for each meq of cation (Ca^{2+} or Mg^{2+}) released initially.

- Secondary carbonate formation happens only "on site" by definition, and leads to the release of 0.5 mol of CO_2 for each meq of cation (Ca^{2+}) precipitated (eq. S9).

Given that we do not have access to water discharge at Séchilienne, this analysis cannot be performed on a flux basis. Therefore, we use a concentration-based analysis, where the CO_2 effect of each process is compared within each spring in a consistent manner and expressed as the consumption or release of CO_2 in mol per liter of water (Fig. 7).

We performed this analysis on all springs but spring S12, for which the significant influence of anthropogenic activities precludes quantitative apportionment by the methods outlined above. In addition, in the cases of springs S20 and S21 none of the 10,000 Monte Carlo runs were able to yield X_i^E values in the interval [0,1] for all i and E. This is probably because their hydrochemistry can be readily explained by a simple binary mixture between gyspum and carbonate-derived solutes, such that any small variation in the composition of these end members result in negative X_{sil}^E values for one or more instances of the element E. However, because the hydrochemistry of springs S20 and S21 is similar to those of S13 and S15, we expect that their role on atmospheric CO_2 is similar to that played by springs S13 and S15 (Fig. 7).

References

Bickle, M. J., Tipper, E. T., Galy, A., Chapman, H., and Harris, N.: On Discrimination Between Carbonate and Silicate Inputs to Himalayan Rivers, Am. J. Sci., 315, 120–166, https://doi.org/10.2475/02.2015.02, 2015

415

Kloppmann, W., Leroux, L., Bromblet, P., Pogam, P.-Y., Cooper, A., Worley, N., Guerrot, C., Montech, A., Gallas, A., Aillaud, R.: Competing English, Spanish, and French alabaster trade in Europe over five centuries as evidenced by isotope fingerprinting. Proceedings of the National Academy of Sciences. 114. 201707450. 10.1073/pnas.1707450114, 2017

420   McArthur, J. and Howarth, R.: Strontium Isotope Stratigraphy. 10.1016/B978-0-444-59425-9.00007-X, 2004

Négrel, P., Allègre, C. J., Dupré, B., Lewin, E.: Erosion sources determined by inversion of major and trace element ratios and strontium isotopic ratios in river: The Congo Basin case, Earth and Planetary Science Letters, 120(1–2), 59–76, https://doi.org/10.1016/0012-821X(93)90023-3, 1993

425

Torres, M. A., West, A. J., Clark, K. E., Paris, G., Bouchez, J., Ponton, C., Adkins, J. F.: The acid and alkalinity budgets of weathering in the Andes–Amazon system: Insights into the erosional control of global biogeochemical cycles. Earth and Planetary Science Letters, 450, 381–391, https://doi.org/10.1016/j.epsl.2016.06.012, 2016

430

435